

Enhanced Photo-Excitation and Angular-Momentum Imprint of Gray Excitons in WSe₂ Monolayers by Spin-Orbit-Coupled Vector Vortex Beams

Oscar Javier Gomez Sanchez^{#,†}, Guan-Hao Peng^{#,*,†}, Wei-Hua Li,[†] Ching-Hung Shih,[‡] Chao-Hsin Chien,[‡] and Shun-Jen Cheng^{*,†}

[†]*Department of Electrophysics, National Yang Ming Chiao Tung University, Hsinchu 300, Taiwan*

[‡]*Institute of Electronics, National Yang Ming Chiao Tung University, Hsinchu 300, Taiwan*

E-mail: bnm852i@gmail.com; sjcheng@nycu.edu.tw

[#] These authors contributed equally to this work and their names are listed by alphabetical order.

Abstract

A light beam can be spatially structured in the complex amplitude to possess orbital angular momentum (OAM), which introduces an extra degree of freedom alongside the intrinsic spin angular momentum (SAM) associated with circular polarization. Furthermore, super-imposing two such twisted light (TL) beams with distinct SAM and OAM produces a vector vortex beam (VVB) in non-separable states where not only complex amplitude but also polarization are spatially structured and entangled with each other. In addition to the non-separability, the SAM and OAM in a VVB are intrinsically coupled by the optical spin-orbit interaction and constitute the profound spin-orbit physics in photonics. In this work, we present a comprehensive theoretical investigation, implemented on the first-principles base, of the intriguing light-matter interaction between VVBs and WSe₂ monolayers (WSe₂-MLs), one of the best-known and promising two-dimensional (2D) materials in optoelectronics dictated by excitons, encompassing bright exciton (BX) as well as various dark excitons (DXs). One of the key findings of our study is that a substantial enhancement of the photo-excitation of gray excitons (GXs), a type of spin-forbidden dark exciton, in a WSe₂-ML can be achieved through the utilization of a 3D-structured TL with the optical spin-orbit interaction. Moreover, we show that a spin-orbit-coupled VVB surprisingly allows for the imprinting of the carried optical information onto gray excitons in 2D materials, which is robust against the decoherence mechanisms in materials. This suggests a promising method for deciphering the transferred angular momentum from structured lights to excitons.

Keywords

gray exciton, two-dimensional materials, transition-metal dichalcogenide, twisted light, vector vortex beam, WSe₂.

A spatially structured light beam with a cylindrically twisted phase front introduces quantized orbital angular momenta (OAM), $L_z = \ell\hbar$, which serves as an extra degree of freedom for light alongside spin angular momentum (SAM), $S_z = \sigma\hbar$, where $\sigma = \pm 1$ represents the right- or left-handed circular polarization of light.¹⁻⁴ Such a cylindrically structured beam, also referred to as twisted light (TL) or optical vortex (OV), is denoted by $|\sigma, \ell\rangle$ and characterized by an unbounded quantum number ℓ has been demonstrated advantageous in a variety of advanced photonic and quantum applications, ranging from optical tweezers,^{5,6} optical trapping,^{7,8} high-resolution optical microscope,⁹⁻¹¹ optical communication,^{12,13} to high dimensional quantum information.¹⁴⁻¹⁷ Besides, the co-existence of SAM and OAM in a structured light beam gives rise to intriguing optical spin-orbit-coupled phenomena,¹⁸⁻²⁰ including photonic spin Hall effect,²¹⁻²⁴ spin-based plasmonics,²⁵ photonic wheel,^{26,27} optical transverse spin,²⁸ and longitudinal field of light.²⁹⁻³³

Furthermore, a structured light beam can be tailored by the controlled superposition of TLs with distinct SAM and OAM, expressed by

$$|\sigma, \ell, \sigma', \ell'; \alpha, \beta\rangle = \cos(\beta/2) |\sigma, \ell\rangle + e^{i\alpha} \sin(\beta/2) |\sigma', \ell'\rangle, \quad (1)$$

where α (β) determines the relative phase (weight) of the two TL components in the superposition state and represents the azimuthal (polar) angle in the Poincaré sphere representation.³⁴⁻³⁷ The structured light described by Eq. (1) forms a vector vortex beam (VVB) in non-separable states, where not only the complex amplitude but also the polarization of light are spatially structured and entangled with each other.^{35,37-40} The exceptional characteristics of VVBs as light sources have been demonstrated to enable advanced photonics applications,⁴¹ particle acceleration,^{42,43} vector beam multiplexing communication,^{44,45} high dimensional quantum entanglement,^{46,47} and vector vortex quantum steering.⁴⁸ The non-separability of the SAM and OAM, further coupled by the optical spin-orbit interaction (SOI), in a VVB em-

bodies the profound spin-orbit physics of optics and naturally affect its interaction with matters, which, however, remain largely unexplored so far. Following the rapid advancement in the TL-based optics, it is certainly crucial to investigate the physics of the interaction between structured lights and seek the emergent nano-materials suited for the prospective TL-based optoelectronics.⁴⁹⁻⁵³ Specifically, identifying materials that facilitate efficient transfer of optical angular momenta from structured light and enable deciphering of transmitted optical information is highly desirable for prospective TL-based optoelectronics.

Atomically thin transition-metal dichalcogenide monolayer (TMD-ML) is one of the most promising optoelectronic 2D materials with superior light-matter interactions that are dictated by excitons.⁵⁴⁻⁵⁸ In TMD-MLs, excitons are strongly bound by the enhanced Coulomb interaction, leading to the atypical band dispersion and exciton fine structures associated with the diverse degrees of freedom inherent in excitons, including spin and valley properties as well as the center-of-mass motion of exciton.⁵⁹⁻⁶³ The pronounced exciton fine structure of a TMD-ML enables the unambiguous spectral resolution of diverse exciton complexes, such as the bright exciton and various dark exciton states,⁶⁴ each possessing distinct degrees of freedom. In darkish W-based TMD-MLs, e.g. WSe₂,⁶⁵ the intravalley repulsive exchange energy combined with the conduction band splitting shifts the dipole-allowed bright exciton states upwards by tens of meV and leave the spin-forbidden dark exciton doublet as the excitonic ground states.⁶⁶ Furthermore, the lowest doublet of dark excitons undergoes valley-mixing, resulting from weak intervalley exchange interaction, and exhibits a slight energy splitting, yielding a completely dark exciton and a slightly optically active state known as a gray exciton (GX).⁶⁷⁻⁶⁹

Notably, GXs have recently garnered significant attention due to their possession of the both advantages from bright excitons (BXs) as well as dark excitons (DXs), i.e. long lifetime and brightness.^{62,70} These characteristics are highly desirable for future exciton-based quan-

tum technologies and devices.^{71,72} Nevertheless, optically accessing the GX states remains a non-trivial task and usually needs the additional aid of external fields or post-processed structures of samples, such as in-plane magnetic fields,^{65,69,73} plasmonic fields,⁷⁴ or photonic crystals in close proximity.^{62,75} Despite the out-of-plane dipole and the expected light emission along the plane of 2D materials, direct observation of GXs in TMD-MLs has been shown to be achievable by using high numerical aperture objectives in both regular photoluminescence (PL) spectroscopies^{76,77} where the detectors are set in the normal direction to the 2D materials, and angle-resolved optical spectroscopies. The fascinating attributes of TL have recently stimulated a few pioneering investigations concerning their interactions with BXs in 2D systems.^{50,78–86} However, beyond scalar optical vortex beams or TLs, the interplay between VVBs and excitons in 2D materials remains an appealing but yet largely unexplored area.

In this study, we present a comprehensive theoretical investigation based on first-principles, focusing on the interaction between spin-orbit-coupled VVBs and exciton states in a WSe₂-ML, including both BXs and GXs. We reveal that structured lights can serve as an exceptional light source enabling optically enhance the photo-excitation of GXs in a WSe₂-ML through the coupling of the longitudinal field component associated with the SOI. Furthermore, we show that a spin-orbit-coupled VVB enables the imprinting of optical information onto the optical transitions of GXs in the 2D materials.

RESULTS AND DISCUSSION

The vector potential of a circularly polarized Laguerre-Gaussian (LG) TL in the fundamental radial mode $p = 0$ under the Coulomb gauge is $\mathbf{A}^{\sigma,\ell}(\mathbf{r}) = e^{iq_0z} \mathbf{A}^{\sigma,\ell}(\boldsymbol{\rho}) = e^{iq_0z} [\hat{\boldsymbol{\epsilon}}_{\parallel}^{\sigma} A_{\parallel}^{\ell}(\boldsymbol{\rho}) + \hat{\boldsymbol{\epsilon}}_z A_z^{\sigma,\ell}(\boldsymbol{\rho})]$, (see Supporting Information for details) being a 3D-structured light with the both transverse and longitudinal components⁸⁷ as il-

lustrated in Fig. 1(a), where $\mathbf{r} = (x, y, z) = (\boldsymbol{\rho}, z)$ is the position vector, $\hat{\boldsymbol{\epsilon}}_{\parallel}^{\sigma} = \frac{1}{\sqrt{2}}(\hat{\mathbf{x}} + i\sigma\hat{\mathbf{y}})$ is the transverse polarization vector labelled by the optical helicity $\sigma = \pm 1$, $\hat{\boldsymbol{\epsilon}}_z = \hat{\mathbf{z}}$ is the longitudinal polarization vector, $\ell = 0, \pm 1, \pm 2, \pm 3, \dots$ is the index of the azimuthal mode of light,⁸⁸ $q_0 = 2\pi n_{rf}/\lambda$ is the wave number of light propagating along the z -direction, λ is the wavelength of light in vacuum, and n_{rf} is the refractive index of material. In the formalism of vector potential, the spin part of light is associated with the transverse vector of polarization, $\hat{\boldsymbol{\epsilon}}_{\parallel}^{\sigma}$, and the orbital part of light is characterized by the scalar function of the vector potential, $A_{\parallel}^{\ell}(\boldsymbol{\rho})$. Throughout this work, we consider the TL with the beam waist, $w_0 = 1.5 \mu\text{m}$. The vector potential of a structured light beam in general varies along, besides the in-plane direction, the z -direction as well. However, within a narrow z -range characterized by the Rayleigh length, z_R , the z -dependence of vector potential is very weak and one can adopt the long Rayleigh length approximation to neglect the z -dependence of vector potential. Without loss of generality, we simply consider $n_{rf} = 1$ for most studies in this work. For the TL with $w_0 = 1.5 \mu\text{m}$ and the resonant frequency to the exciton transition energy of $E_{B\pm,0}^X = 1.7 \text{ eV}$,^{89,90} the Rayleigh length for the TL is estimated as $z_R = 11.81 \mu\text{m}$ according to the relationship between light speed c , light wavevector q_0 , resonant excitation energy $\hbar c q_0 = E_{B\pm,0}^X$, and the definition of Rayleigh length $z_R = q_0 w_0^2/2$.^{89,90} Considering the nm-scaled thickness of 2D materials $d \ll z_R$,⁹¹ we adopt the long Rayleigh length approximation and disable the variable z in the vector potential throughout this work. As stated in Sec. SII.B of the Supporting Information, the TL with a smaller Rayleigh length, z_R , will give rise to the enhanced longitudinal component and higher transition rates for GXs.

For the integration with the light-matter interaction based on the exciton band structures of 2D materials, it is necessary to transform the vector potentials into the angular spectrum representation through a 2D Fourier transform. The Fourier transform of the complex transverse component of $\mathcal{A}^{\sigma,\ell}(\mathbf{q}_{\parallel}) \equiv$

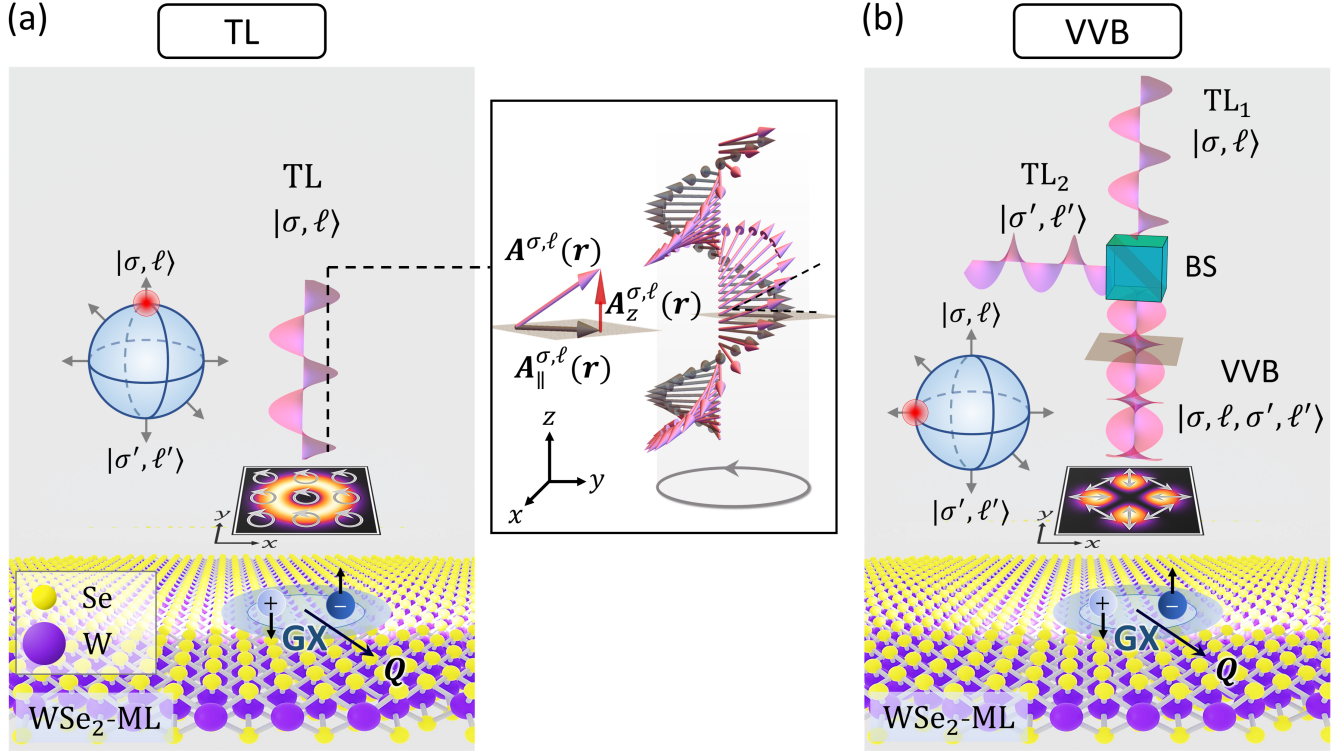


Figure 1: (a) The schematic of a single twisted light (TL) in the state $|\sigma, \ell\rangle$ normally incident on a WSe_2 monolayer (WSe_2 -ML), where σ and ℓ represent the spin angular momentum (SAM) and orbital angular momentum (OAM) carried by the TL, respectively. The panel on the right-hand side shows that the polarization of a TL (pink arrow line) is not purely transverse (gray arrow line), $\mathbf{A}_{\parallel}^{\sigma, \ell}(\mathbf{r}) = e^{iq_0 z} A_{\parallel}^{\ell}(\boldsymbol{\rho}) \hat{\mathbf{e}}_{\parallel}^{\sigma}$, but also contains a small longitudinal field component (red arrow line), $\mathbf{A}_z^{\sigma, \ell}(\mathbf{r}) = e^{iq_0 z} A_z^{\ell}(\boldsymbol{\rho}) \hat{\mathbf{e}}_z$, resulting from the optical spin-orbit interaction (SOI). Below the TL, the small square panel displays the contour plot of the squared magnitude of the longitudinal component of the vector potential and the in-plane circular polarizations (white arrow lines) of the TL, where the polarization remains fixed over the in-plane. The schematic on the left-hand side illustrates that the TL state, $|\sigma, \ell\rangle$, is located at the north pole of the Poincaré sphere. (b) The schematic of a vector vortex beam (VVB) superimposed by two TLs, $|\sigma, \ell\rangle$ and $|\sigma', \ell'\rangle$, normally incident on a WSe_2 -ML. BS stands for beam splitter. Below the VVB, the small square panel displays the contour plot of the squared magnitude of the longitudinal component of the vector potential and the in-plane polarizations of the VVB, both of which are spatially varied, unlike a TL. The VVB here is a state located at the equator of the Poincaré sphere, i.e. $|\sigma, \ell, \sigma', \ell'\rangle \equiv |\sigma, \ell, \sigma', \ell'; \alpha = 0, \beta = \pi/2\rangle$ (see Eq. (1) for the definition).

$\frac{1}{\Omega} \int d^2 \boldsymbol{\rho} \mathbf{A}^{\sigma, \ell}(\boldsymbol{\rho}) e^{-i \mathbf{q}_{\parallel} \cdot \boldsymbol{\rho}} = \hat{\boldsymbol{\varepsilon}}_{\parallel}^{\sigma} \mathcal{A}_{\parallel}^{\ell}(\mathbf{q}_{\parallel}) + \hat{\boldsymbol{\varepsilon}}_z \mathcal{A}_z^{\sigma, \ell}(\mathbf{q}_{\parallel})$
is derived as

$$\mathcal{A}_{\parallel}^{\ell}(\mathbf{q}_{\parallel}) = \tilde{F}_{|\ell|}(q_{\parallel}) e^{i \ell \phi_{\mathbf{q}}}, \quad (2)$$

and the longitudinal one as

$$\mathcal{A}_z^{\sigma, \ell}(\mathbf{q}_{\parallel}) \approx -(\hat{\boldsymbol{\varepsilon}}_{\parallel}^{\sigma} \cdot \hat{\mathbf{q}}) \mathcal{A}_{\parallel}^{\ell}(\mathbf{q}_{\parallel}), \quad (3)$$

as detailed in section SII of Supporting Information, where Ω is the area of the system, $\hat{\mathbf{q}} = \mathbf{q}/|\mathbf{q}|$ with $\mathbf{q} = (\mathbf{q}_{\parallel}, q_0)$, $\mathbf{q}_{\parallel} = (q_x, q_y)$, and $\phi_{\mathbf{q}} = \tan^{-1}(q_y/q_x)$. The expression for the complex-valued radial function can be represented as $\tilde{F}_{|\ell|}(q_{\parallel}) = (-i)^{|\ell|} F_{|\ell|}(q_{\parallel})$, where the detailed description of the amplitude function $F_{|\ell|}(q_{\parallel})$ is provided in Supporting Information.⁸⁴ In turn, the vector potential as a function of coordinate position in the real space can be expressed as $\mathbf{A}^{\sigma, \ell}(\boldsymbol{\rho}) = \sum_{\mathbf{q}_{\parallel}} \mathcal{A}^{\sigma, \ell}(\mathbf{q}_{\parallel}) e^{i \mathbf{q}_{\parallel} \cdot \boldsymbol{\rho}}$, via the inverse Fourier transform.^{50,84}

The appearance of $\mathcal{A}_{\parallel}^{\ell}(\mathbf{q}_{\parallel})$ in Eq. (3) accounts for that the longitudinal field in a TL fully inherits the OAM-encoded transverse spatial structures described by Eq. (2). Notably, the term $(\hat{\boldsymbol{\varepsilon}}_{\parallel}^{\sigma} \cdot \hat{\mathbf{q}}) = (\hat{\boldsymbol{\varepsilon}}_{\parallel}^{\sigma} \cdot \mathbf{q}_{\parallel})/q$ appearing in Eq. (3) manifests itself as the optical SOI that couples the optical spin ($\hat{\boldsymbol{\varepsilon}}_{\parallel}^{\sigma}$) and the in-plane momentum component (\mathbf{q}_{\parallel}) carried by the longitudinal field. Alternatively, $(\hat{\boldsymbol{\varepsilon}}_{\parallel}^{\sigma} \cdot \hat{\mathbf{q}}) = \frac{\sin \theta_{\mathbf{q}}}{\sqrt{2}} e^{i \sigma \phi_{\mathbf{q}}}$ with $\sin \theta_{\mathbf{q}} \equiv \frac{q_{\parallel}}{\sqrt{q_{\parallel}^2 + q_0^2}}$ can be expressed in the spherical coordinates, showing that the optical spin σ is fully transferred to the longitudinal field and the strength of optical SOI increases with increasing q_{\parallel} . Combining $\mathcal{A}_{\parallel}^{\ell}(\mathbf{q}_{\parallel})$ and $(\hat{\boldsymbol{\varepsilon}}_{\parallel}^{\sigma} \cdot \hat{\mathbf{q}})$, the longitudinal field expressed by Eq. (3) is shown imprinted by $\hbar(\sigma + \ell) \equiv \hbar J$, which is the total angular momentum (TAM) of TL in the paraxial regime.¹⁸

In Supporting Information, Figure S1(a) and (b) [(c) and (d)] show the squared magnitude, the real part, and the imaginary part of the complex vector potential $\mathcal{A}_{\parallel}^{\ell}(\mathbf{q}_{\parallel})$ [$\mathcal{A}_z^{\sigma, \ell}(\mathbf{q}_{\parallel})$], as functions of \mathbf{q}_{\parallel} for the polarized TLs in the LG modes with $p = 0$ and the optical angular momenta, $(\sigma, \ell) = (1, 1)$ and $(\sigma, \ell) = (-1, -1)$, respectively. Basically, the squared magnitudes of the vector potentials of the TLs carrying fi-

nite OAM ($|\ell| > 0$) in the fundamental radial mode ($p = 0$) present ring-shaped distributions over the \mathbf{q}_{\parallel} -plane, whose ring sizes increase with increasing ℓ .⁸⁴ This indicates that the TLs with greater ℓ comprise the more components of large q_{\parallel} and, according to the momentum-conservation law, likely couple the more exciton states with large in-plane momentum, \mathbf{Q} . Moreover, the effects of optical SOI become more important in the TLs with greater ℓ . One also notes that the ring size of the \mathbf{q}_{\parallel} -dependent magnitudes of the longitudinal component, $|\mathcal{A}_z^{\sigma, \ell}(\mathbf{q}_{\parallel})|^2$, is unequal but slightly larger than that of the transverse one, $|\mathcal{A}_{\parallel}^{\ell}(\mathbf{q}_{\parallel})|^2$. With no effects of SOI, the *transverse* component of vector potential is decoupled from SAM (see Eq. (2)) and remains the same for $\sigma = +1$ and $\sigma = -1$. Indeed, the patterns of $\text{Re}(\mathcal{A}_{\parallel}^{\ell=\pm 1}(\mathbf{q}_{\parallel}))$ and $\text{Im}(\mathcal{A}_{\parallel}^{\ell=\pm 1}(\mathbf{q}_{\parallel}))$ in Fig. S1(a.2)-(a.3) and S1(b.2)-(b.3) are shown dumbbell-like to reflect the OAM $\ell = \pm 1$ carried by the TL. As pointed out previously, the longitudinal field in a TL inherits the total angular momentum, $J = \sigma + \ell$, of the light. Thus, as seen in Fig. S1(c.2)-(c.3) and S1(d.2)-(d.3), the in-plane patterns of the real and imaginary parts of $\mathcal{A}_z^{\sigma=\pm 1, \ell=\pm 1}(\mathbf{q}_{\parallel})$ are double-dumbbell-like to reflect the TAM, $J = \sigma + \ell = \pm 2$.

For the studies of exciton, we employ the theoretical methodology developed by Ref.(63, 92) to solve the Bethe-Salpeter equation (BSE) established in first-principles for the exciton fine structure spectra of encapsulated 2D materials (see Supporting Information for details). The exciton states of a 2D material is expressed as $|S, \mathbf{Q}\rangle = \frac{1}{\sqrt{\Omega}} \sum_{v\mathbf{c}\mathbf{k}} \Lambda_{S, \mathbf{Q}}(v\mathbf{c}\mathbf{k}) \hat{c}_{\mathbf{c}\mathbf{k}+\mathbf{Q}}^{\dagger} \hat{h}_{v-\mathbf{k}}^{\dagger} |GS\rangle$, where Ω is the area of the 2D material, $\hat{c}_{\mathbf{c}\mathbf{k}}^{\dagger}$ ($\hat{h}_{v-\mathbf{k}}^{\dagger}$) is defined as the particle operator creating the electron (hole) of wavevector \mathbf{k} ($-\mathbf{k}$) in conduction band c (valence band v), $|GS\rangle$ denotes the ground state of the material, $\Lambda_{S, \mathbf{Q}}(v\mathbf{c}\mathbf{k})$ is the amplitude of the electron-hole configuration $\hat{c}_{\mathbf{c}\mathbf{k}+\mathbf{Q}}^{\dagger} \hat{h}_{v-\mathbf{k}}^{\dagger} |GS\rangle$ and corresponds to the solution of the BSE for the exciton in momentum space, S is the band index of the exciton state, \mathbf{Q} is the center-of-mass momentum of exciton. For a WSe₂-ML, the DX states as

the exciton ground states are significantly lower than the bright ones by ~ 48.8 meV, as shown in Fig. 2(b)-(c) and 3(a).^{93,94} The calculated BX-DX fine structure is in excellent agreement with the experimental observation.⁶³ Carefully examining the lowest DX states, one notes a small splitting between the DX doublet resulting. Combined with the SOI of quasi-particle, the inter-valley exchange interaction splits the lowest DX doublet and turns one of them, referred to as gray exciton (GX), to be slightly bright.⁶⁸ With finite \mathbf{Q} , the inter-valley e - h exchange interaction splits the valley exciton BX bands into a quasi-linear upper, $|B+, \mathbf{Q}\rangle$, and parabolic lower band, $|B-, \mathbf{Q}\rangle$.^{50,95-98} At the light cone edge where $|\mathbf{Q}| = q_0 \approx Q_c$, the valley splitting between the upper and lower BX bands is merely a few meV, much smaller than the energy separation of BX and DX/GX states. The transition dipole moment of an exciton state is evaluated by $\mathbf{D}_{S,\mathbf{Q}}^X = \frac{1}{\sqrt{\Omega}} \sum_{v\mathbf{c}\mathbf{k}} \Lambda_{S,\mathbf{Q}}(v\mathbf{c}\mathbf{k}) \mathbf{d}_{v\mathbf{k},c\mathbf{k}}$, where $\mathbf{d}_{v\mathbf{k},c\mathbf{k}} \equiv e \langle \psi_{v\mathbf{k}} | \mathbf{r} | \psi_{c\mathbf{k}} \rangle = \frac{e\hbar}{im_0(\epsilon_{v\mathbf{k}} - \epsilon_{c\mathbf{k}})} \langle \psi_{v\mathbf{k}} | \mathbf{p} | \psi_{c\mathbf{k}} \rangle$ is the dipole moment of single-electron transition evaluated by using the first-principles package Quantum Espresso and the Wannier90 package, as presented in Sec. SI.C of Supporting Information,^{92,96,99,100} with \mathbf{p} the operator of linear momentum, m_0 ($|e|$) the electron rest mass (the elementary charge), and $\epsilon_{n\mathbf{k}}$ the energy of the Bloch state characterized by the band index n and wavevector \mathbf{k} . The first-principles-calculated quasi-particle band structure of a WSe₂-ML is shown in Fig. 2(a). The first-principles-calculated \mathbf{Q} -dependent in-plane and out-of-plane projections of the transition dipole of the exciton states in the fine structure of WSe₂-ML are shown in Fig. 2(b) and 2(c), respectively.

The numerically calculated transition dipole moments of the BX (GX) states are shown mainly in-plane (out-of-plane) oriented, as presented by Fig. 2(b) and (c). In addition to the strong exciton-photon interaction, the fine structure spectrum of a WSe₂-ML consisting of various exciton states with distinctly oriented dipoles serves as an excellent test bed to explore the distinct field components in the 3D-structured lights. In turn, TLs carrying con-

trolled SAM and OAM enable us to selectively access and distinguish a variety of exciton states of 2D materials.

In the widely-used exciton pseudo-spin model that neglects the slight variations of dipole moments with respect to \mathbf{Q} , the transition dipoles of the upper BX, lower BX, and GX states are described by $\mathbf{D}_{B+, \mathbf{Q}}^X \approx D_{B+, 0}^X \hat{\mathbf{Q}}$, $\mathbf{D}_{B-, \mathbf{Q}}^X \approx D_{B-, 0}^X \hat{\mathbf{Q}}_{\perp}$, and $\mathbf{D}_{G, \mathbf{Q}}^X \approx D_{G, 0}^X \hat{\mathbf{z}}$, respectively, where $\hat{\mathbf{Q}} = \mathbf{Q}/|\mathbf{Q}|$, $\hat{\mathbf{Q}}_{\perp} = -\sin \phi_{\mathbf{Q}} \hat{\mathbf{x}} + \cos \phi_{\mathbf{Q}} \hat{\mathbf{y}}$ ($\hat{\mathbf{Q}}_{\perp} \cdot \hat{\mathbf{Q}} = \hat{\mathbf{Q}}_{\perp} \cdot \hat{\mathbf{z}} = 0$), and $D_{B\pm, \mathbf{Q}}^X$ ($D_{G, \mathbf{Q}}^X$) is the magnitude of the dipole moment of BX (GX). With the fixed magnitude of the exciton dipole, the energy band dispersion of BX doublet split by the long-ranged exchange interaction can be explicitly solved and shown in Fig. 3(a) in comparison with the first-principles-calculated results.

In the time-dependent perturbation theory, the Hamiltonian of light-matter interaction with respect to a light described by the vector potential $\mathbf{A}(\mathbf{r})$ is given by $H_{LMI} \approx \frac{|e|\hbar}{2m_0} \mathbf{A}(\mathbf{r}) \cdot \mathbf{p}$ in the weak field and rotating wave approximations.¹⁰² The first-order perturbed exciton state could be expressed as⁸⁴

$$|\Psi^X\rangle \approx |GS\rangle + \sum_{S\mathbf{Q}} \tilde{c}_{S,\mathbf{Q}} e^{-iE_{S,\mathbf{Q}}^X t/\hbar} |S, \mathbf{Q}\rangle, \quad (4)$$

where $\tilde{c}_{S,\mathbf{Q}} = \tilde{c}_{S,\mathbf{Q}}(t)$ is the time-dependent coefficient of the exciton state, $|S, \mathbf{Q}\rangle$. As shown in Eq. (4), the exciton state photo-excited by a structure light will be in the exciton superposition state, which is superimposed by the states of individual finite-momentum exciton, $|S, \mathbf{Q}\rangle$, with the complex coefficient that is shown to be proportional to the optical matrix element $\tilde{c}_{S,\mathbf{Q}} \propto \tilde{M}_{S,\mathbf{Q}}$. The optical matrix element of an exciton state, $|S, \mathbf{Q}\rangle$, is derived as $\tilde{M}_{S,\mathbf{Q}}^{\sigma,\ell} = \frac{1}{\sqrt{\Omega}} \sum_{v\mathbf{c}\mathbf{k}} \Lambda_{S,\mathbf{Q}}^*(v\mathbf{c}\mathbf{k}) \langle \psi_{c\mathbf{k}+\mathbf{Q}} | \frac{|e|\hbar}{2m_0} \mathbf{A}^{\sigma,\ell}(\mathbf{r}) \cdot \mathbf{p} | \psi_{v\mathbf{k}} \rangle$,⁸⁴ which measures the amplitude of the optical transition of the exciton state, $|S, \mathbf{Q}\rangle$, induced by the incident TL carrying the angular momenta σ and ℓ . In terms of the optical matrix element, the Fermi's golden rule formulates the rate of incoherently photo-exciting the finite-momentum exciton state, $|S, \mathbf{Q}\rangle$, by using

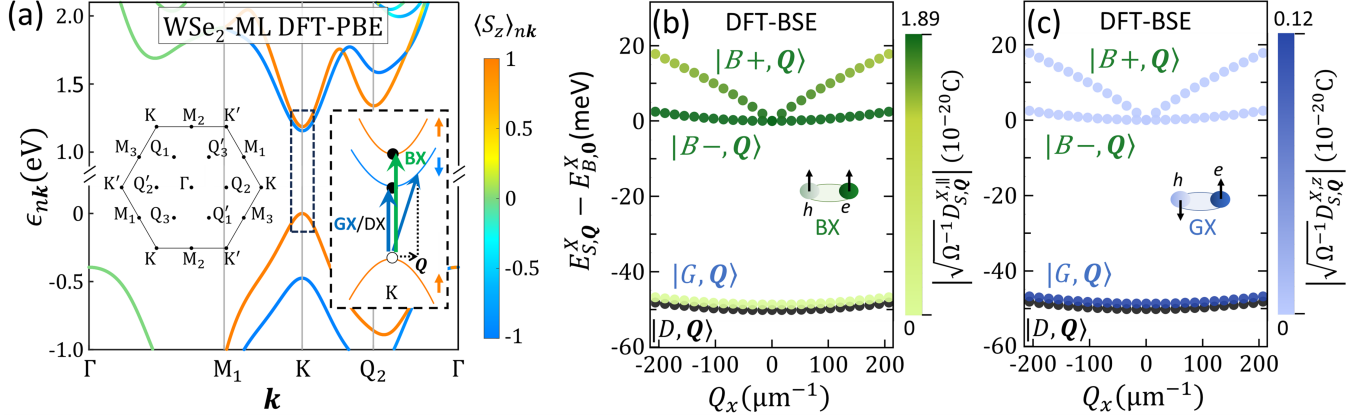


Figure 2: (a) The spin-resolved quasi-particle band structure of a WSe₂-ML calculated by using the first-principles package Quantum Espresso with the PBE functional in DFT. The color of bands is mapped to the spin z -component of the Bloch states, $\langle S_z \rangle_{n\mathbf{k}} = \langle \psi_{n\mathbf{k}} | \sigma_z | \psi_{n\mathbf{k}} \rangle$, where σ_z is the Pauli matrix. The left inset shows the first Brillouin zone of TMD-MLs. The dashed rectangular box is the enlarged view of the lowest spin-split conduction bands and the topmost valence band at K -valley, where the green arrow line indicates the transitions of spin-allowed bright exciton (BX), the blue arrow line indicates the transition of spin-forbidden gray (GX) and dark exciton (DX), and the tilted arrow line indicates the transition of the exciton with a finite center-of-mass momentum, \mathbf{Q} . (b) The calculated 1s-exciton band structure, on the Q_x -axis, of a WSe₂-ML sandwiched by semi-infinite hBN layers obtained by solving the first-principles-based BSE, comprising the valley-split BX states, $|B\pm, \mathbf{Q}\rangle$, and the lowest GX and DX states, $|G, \mathbf{Q}\rangle$ and $|D, \mathbf{Q}\rangle$. The exciton bands are offset by the energy of BX at $\mathbf{Q} = \mathbf{0}$. The gradient green colors of the exciton states are mapped to the in-plane component of the transition dipole ($D_{S,\mathbf{Q}}^X = D_{S,\mathbf{Q}}^{X,\parallel} + D_{S,\mathbf{Q}}^{X,z} \hat{z}$) of exciton, $|D_{S,\mathbf{Q}}^{X,\parallel}|$. (c) shows the same exciton band structure as (b), but presents the out-of-plane component of the transition dipoles, $|D_{S,\mathbf{Q}}^{X,z}|$, using gradient blue colors.

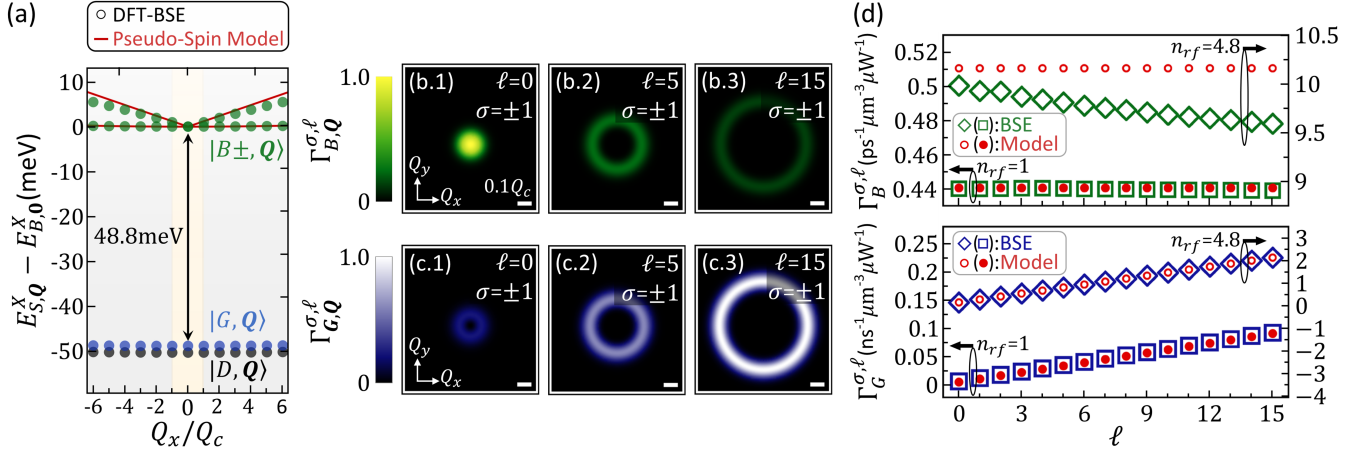


Figure 3: (a) The exciton fine structure of the low-lying exciton states along the Q_x axis around the vicinity of the light-cone reciprocal range, comprising the valley-split bright exciton bands (green circles) and the lowest gray (blue circles) and dark exciton ones (black circles). $Q_c = E_{B\pm,0}^X/\hbar c$ is defined as the light-cone radius. For comparison, the band dispersions of BX states simulated by using the pseudo-spin model (red line) that consider a fixed value for the dipole of BX are presented. (b1)-(b3) Density plots of the optical transition rates, $\Gamma_{B,Q}^{\sigma,\ell}$ as functions of \mathbf{Q} for the finite momentum BX states of a WSe₂-ML under the excitation of polarized TLs with the SAM and OAM, $(\sigma, \ell) = (\pm 1, 0), (\pm 1, 5)$ and $(\pm 1, 15)$, respectively. (c1)-(c3) Density plots of $\Gamma_{G,Q}^{\sigma,\ell}$ for the TL-excited finite-momentum GX states. All of the contour plots follow the same color-map on the leftmost side. For reference, the length of the horizontal bar in white color represents the magnitude of $0.1Q_c$. (d) The total transition rates of the TL-excited superposition states of BX (empty green squares) and GX states (empty blue squares) as a function of the ℓ of the TL, calculated by taking the exciton band structure obtained by solving the first-principles-based BSE from (a). For a more realistic simulation, the effective refractive index of TMD-MLs,¹⁰¹ $n_{rf} = 4.8$, that shortens the wavelength of light in materials ($q_0 \rightarrow n_{rf}q_0$ and $Q_c \rightarrow n_{rf}Q_c$) is considered for comparison, as illustrated by the empty green and blue diamonds for BXs and GXs, respectively. In model simulations, where a fixed dipole value is assumed, the results for $n_{rf} = 1$ and $n_{rf} = 4.8$ are shown by the filled and empty red circles, respectively.

a TL with (σ, ℓ) as

$$\Gamma_{S, \mathbf{Q}}^{\sigma, \ell} = \frac{2\pi}{\hbar} |\tilde{M}_{S, \mathbf{Q}}^{\sigma, \ell}|^2 \rho(\hbar\omega = E_{S, \mathbf{Q}}^X), \quad (5)$$

where $\rho(\hbar\omega)$ is the density of states of light in the range of angular frequency between ω and $\omega + d\omega$. The incoherence nature of the Fermi's golden rule can be better understood in the density matrix representation of wavefunction, which defines the density matrix element $\rho_{S, \mathbf{Q}; S', \mathbf{Q}'} \equiv \tilde{c}_{S, \mathbf{Q}} \tilde{c}_{S', \mathbf{Q}'}^*$.¹⁰³ Thus, in the incoherent time-dependent perturbation theory, the transition rate of the exciton superposition state can be counted by summing all the transition probabilities of $|S, \mathbf{Q}\rangle$, which is measured by the real-valued diagonal element of the density matrix for the superposition states, i.e. $\rho_{S, \mathbf{Q}; S, \mathbf{Q}} = |\tilde{c}_{S, \mathbf{Q}}|^2 \propto |\tilde{M}_{S, \mathbf{Q}}^{\sigma, \ell}|^2$.

In the electric dipole approximation, one derives

$$\tilde{M}_{S, \mathbf{Q}}^{\sigma, \ell} \approx \frac{E_g}{2i\hbar} \mathcal{A}^{\sigma, \ell}(\mathbf{Q}) \cdot \mathbf{D}_{S, \mathbf{Q}}^{X*}, \quad (6)$$

where $\mathcal{A}^{\sigma, \ell}(\mathbf{Q}) = \hat{\epsilon}_{\parallel}^{\sigma} \mathcal{A}_{\parallel}^{\ell}(\mathbf{Q}) + \hat{\epsilon}_z \mathcal{A}_z^{\sigma, \ell}(\mathbf{Q})$ is the Fourier transform of the vector potential of structured light with the transverse and longitudinal components as given by Eqs. (2) and (3), respectively, $E_g = \epsilon_{c_1 \mathbf{K}/\mathbf{K}'} - \epsilon_{v_1 \mathbf{K}/\mathbf{K}'}$ is the energy gap of the material at the \mathbf{K}/\mathbf{K}' point, and c_1 (v_1) is the lowest conduction (topmost valence) band. The interaction between TL and excitons is characterized by the optical matrix element of Eq. (6). This element involves the inner product of the optical polarization vector, $\hat{\epsilon}_{\parallel}^{\sigma}$ and $\hat{\epsilon}_z$, and the exciton dipole, $\mathbf{D}_{S, \mathbf{Q}}^X$, which is further weighted by the \mathbf{Q} -dependent scalar functions, $\mathcal{A}_{\parallel}^{\ell}(\mathbf{Q})$ and $\mathcal{A}_z^{\sigma, \ell}(\mathbf{Q})$. Basically, the inner product $\hat{\epsilon} \cdot \mathbf{D}_{S, \mathbf{Q}}^{X*}$ (with $\hat{\epsilon} = \hat{\epsilon}_{\parallel}^{\sigma}$ or $\hat{\epsilon} = \hat{\epsilon}_z$) in Eq. (6) remains the same form for both TLs and regular non-structured lights. However, the scalar functions $\mathcal{A}_{\parallel}^{\ell}(\mathbf{Q})$ and $\mathcal{A}_z^{\sigma, \ell}(\mathbf{Q})$, which reflect the spatial structures of TLs, will impose a weighting on the optical matrix element for a finite-momentum exciton state, $|S, \mathbf{Q}\rangle$. This indicates that under the electric dipole approximation, the optical selection rules for a specific state $|S, \mathbf{Q}\rangle$ that are generally determined by $\hat{\epsilon} \cdot \mathbf{D}_{S, \mathbf{Q}}^{X*}$ remain unchanged for both TLs and

regular non-structured lights, but the spatial structures of TLs will directly affect the weighting of the exciton state component, $|S, \mathbf{Q}\rangle$, with the center-of-mass momentum \mathbf{Q} in the exciton superposition state (see Eq. (4)). In other words, the spin part (polarization) of the light directly couples with the dipole of exciton that is related to the relative coordinate of exciton, while the orbital part of the light couples the center-of-mass movement of the exciton.¹⁰⁴

Deriving optical selection rules for exciton states under TL excitation is not a trivial task. The complexity arises because TL-excited superposition states, as detailed in Eq. (4), involve finite-momentum exciton states that do not align with high-symmetry points in reciprocal space. The pioneering work in Ref. (105) analyzed the optical selection rules for BX and GX states in 2D materials under single TL excitation, but applied its group theory analysis only to zero-momentum exciton states. In contrast, our work inherently includes the complete symmetries of finite-momentum exciton states by considering the crystal symmetries within the crystal structures during our first-principles computations.

The optical matrix elements of Eq. (6) for BX and GX states under the excitation of a TL in the LG mode with (σ, ℓ) are derived in the cylindrical coordinate and explicitly shown as below,

$$\tilde{M}_{B\pm, \mathbf{Q}}^{\sigma, \ell} \approx (i\sigma)^{(1\mp 1)/2} \frac{E_g}{2\sqrt{2}i\hbar} \tilde{F}_{|\ell|}(Q) \mathbf{D}_{B\pm, \mathbf{Q}}^X e^{i(\sigma+\ell)\phi_{\mathbf{Q}}} \quad (7)$$

and

$$\tilde{M}_{G, \mathbf{Q}}^{\sigma, \ell} \approx -\frac{E_g}{2\sqrt{2}i\hbar} \tilde{F}_{|\ell|}(Q) \mathbf{D}_{G, \mathbf{Q}}^X e^{i(\sigma+\ell)\phi_{\mathbf{Q}}} \sin \theta_{\mathbf{Q}}, \quad (8)$$

where the exponential term $e^{i(\sigma+\ell)\phi_{\mathbf{Q}}}$ accounts for the TAM transfer from a TL to a GX and the term $\sin \theta_{\mathbf{Q}} \equiv \frac{Q}{\sqrt{Q^2 + q_0^2}}$ arises from the SOI, which makes a normally incident TL forbidden to excite a GX with $Q = 0$ but enhances the photo-generate of GX states with large Q as increasing ℓ .

The exciton fine structure splitting in 2D materials should be an essential material property in the transfer of optical information encoded in a VVB. With the relatively large splitting between BX and GX states,¹⁰⁶ the GX states of a W-based TMD-ML are particularly advantageous for receiving the optical information carried by VVBs since they are unlikely to mix with the high-lying BX states to mess up the received optical information. In contrast, in Mo-based TMD-MLs, the energy levels of the GX states are usually very close to those of dipole-allowed BX states, typically with a small energy separation of a few meV.^{69,107} As compared with W-based TMD-MLs, the small energy separation between BX and GX states of Mo-based TMD-MLs might set an uncertainty in the preservation of the optical information imprinted onto GX states in 2D materials.

Since the valley splitting between the lower and upper BX bands is merely a few meV and normally spectrally unresolvable, as seen in Fig. 3(a),¹⁰⁸ the total transition rate of the BX doublet, $|B\pm, \mathbf{Q}\rangle$, under the photo-excitation of a TL can be counted by $\Gamma_{B,\mathbf{Q}}^{\sigma,\ell} \equiv \sum_{S=B\pm} \Gamma_{S,\mathbf{Q}}^{\sigma,\ell} \propto \sum_{S=B\pm} |\tilde{M}_{S,\mathbf{Q}}^{\sigma,\ell}|^2$. By contrast, a GX state is normally spectrally well apart from the BX states and its transition rate is evaluated by $\Gamma_{G,\mathbf{Q}}^{\sigma,\ell} \propto |\tilde{M}_{G,\mathbf{Q}}^{\sigma,\ell}|^2$.

Figure 3(b) and (c) show the density plots of the optical transition rates, $\Gamma_{B,\mathbf{Q}}^{\sigma,\ell}$ and $\Gamma_{G,\mathbf{Q}}^{\sigma,\ell}$, as functions of \mathbf{Q} for the finite-momentum BX and GX states of a WSe₂-ML incident by polarized TLs with $(\sigma, \ell) = (\pm 1, 0)$, $(\pm 1, 5)$ and $(\pm 1, 15)$, respectively. Overall, the $\Gamma_{B/G,\mathbf{Q}}^{\sigma,\ell}$ for the non-zero $\ell = 5, 15$ exhibit similar ring-shaped patterns over the \mathbf{Q} -plane, with the ring sizes increasing with increasing ℓ . This indicates that a TL with greater ℓ enables the photo-generation of the exciton states (both BX and GX ones) with larger Q , whose superposition forms a more localized spatially wave packet as previously pointed out by Ref. (84).

For a comprehensive understanding, it is interesting to figure out how BX and GX states respond differently when excited by the TL with a well-defined OAM but vanishing SAM (such as linear polarization) and the TL with zero OAM and a well-defined SAM (circular po-

larization). The simulation results for this part of the discussion are shown in Fig. S3 of the Supporting Information. For BXs, both types of light result in an isotropic pattern in the transition rates, as depicted in the upper panels of Fig. S3. In contrast, GXs exhibit a notable difference. The lower panels of Fig. S3 show that the pattern of the transition rates for GXs becomes anisotropic when excited by light with well-defined OAM but vanishing SAM, whereas it remains isotropic when excited by light with zero OAM and well-defined SAM. This feature, as seen in the lower panel of Fig. S3(a), can be realized by examining Eq. (3), where the q_{\parallel} -dependent vector potential of the longitudinal field is directly determined by the inner product of $\hat{\mathbf{e}}$ and $\hat{\mathbf{q}}$. In the case of linearly polarized TL, this results in anisotropy in the transition rate pattern of GXs. This clearly demonstrates the distinct effects of polarization (SAM) and spatial vortex (OAM) in structured lights on GXs.

Analytically, one can show that the TL with ℓ mostly likely excite the finite momentum BX state with $Q = q_{\parallel}^{\ell} = \sqrt{2|\ell|}/w_0$, where the squared magnitude of $\mathcal{A}_{\parallel}^{\ell}(\mathbf{Q})$ is maxima so that $\partial|\mathcal{A}_{\parallel}^{\ell}(\mathbf{Q})|^2/\partial Q|_{Q=q_{\parallel}^{\ell}} = 0$. The upper (lower) panel of Fig. 3(d) shows the total transition rate, $\Gamma_{B/G}^{\sigma,\ell} \equiv \sum_{\mathbf{Q}} \Gamma_{B/G,\mathbf{Q}}^{\sigma,\ell}$ as a function of ℓ , of BX (GX), summing up the contributions by all the finite-momentum states excited by the TLs with $\ell = 0, 1, \dots, 15$. Notably, the rate of photo-exciting the GX superposition states, $\Gamma_G^{\sigma,\ell}$, using a TL with ℓ is shown linearly increasing with increasing ℓ , while the rate of photo-exciting the BX ones, $\Gamma_B^{\sigma,\ell}$, remain nearly unchanged against ℓ . Increasing the OAM of the incident TL from $\ell = 1$ to $\ell = 15$, $\Gamma_G^{\sigma,\ell}$ is enhanced by over one order of magnitude. The ℓ -enhanced photo-generation of GX is associated with the term of SOI, $(\hat{\mathbf{e}}_{\parallel}^{\sigma} \cdot \hat{\mathbf{q}}) = \frac{q_{\parallel}}{\sqrt{2(q_{\parallel}^2 + q_0^2)}} e^{i\sigma\phi_{\mathbf{q}}} \approx \frac{1}{\sqrt{2}} \frac{q_{\parallel}}{q_0} e^{i\sigma\phi_{\mathbf{q}}} \propto q_{\parallel}$, in the longitudinal field of TL as expressed by Eq. (3). From $\partial|\mathcal{A}_z^{\sigma,\ell}(\mathbf{Q})|^2/\partial Q|_{Q=\bar{q}_{\parallel}^{\ell}} = 0$, we have $Q = \bar{q}_{\parallel}^{\ell} = \sqrt{2(|\ell| + 1)}/w_0$. Thus, with increasing ℓ of a TL, the in-plane component of momentum, q_{\parallel} , carried by the TL increases, and so do the strength of the optical SOI and the

magnitude of the longitudinal field, $\mathcal{A}_z^{\sigma,\ell}(\mathbf{Q})$, of Eq. (3). In Fig. 3(d), alongside the first-principles calculated results, we also present the model-simulated transition rates (indicated by the filled/empty red circles). Due to the weak momentum dependence of the optical matrix element within the narrow reciprocal area of the light-cone, the first-principles-calculated transition rate of the BX (GX) is slightly lower than (very similar to) the model-simulated ones.

Despite the phase term of TAM, $e^{i(\sigma+\ell)\phi_{\mathbf{Q}}}$, encoded in the complex optical matrix elements of BX and GX states as shown in Eqs. (7) and (8), the phase information is not preserved in the squared magnitude of the optical matrix elements. These squared magnitudes, which measure the optical transition rates of the exciton states under incoherence conditions, cannot show the transferred angular momenta to the exciton states. Numerically, by using the incoherent theory of Fermi's golden rule, we will show that the optical information encoded in the longitudinal field of a VVB at the equator state of Poincaré sphere is still transferable to the GX states. This is because, before the photo-generation of an exciton, the internal interference between two TL components in a VVB occurs in advance and directly encodes the optical information into the real-valued amplitude, rather than the complex phase term, of light. In the manner, the read-out of the imprinted optical information in the GX states by a VVB can be achieved by using the regular optical spectroscopy with angle-resolution, as shown in the later section and Fig. 6.

Superimposing two TLs with distinct SAM ($\sigma' = -\sigma$) and OAM ($\ell \neq \ell'$) forms a VVB, $|\sigma, \ell, \sigma', \ell'; \alpha, \beta\rangle$,^{38,39,109} which is structured in both polarization and amplitudes over the 3D space,¹¹⁰ and is prospective in the frontier photonic applications,¹¹¹ e.g. laser material processes,^{112,113} optical encoding/decoding in communication,¹¹⁴ and microscopy.¹¹⁵ In Fig. 4, the north pole ($\alpha = 0, \beta = 0$) and south pole ($\alpha = 0, \beta = \pi$) represent the TL basis in the single LG modes, which are $|\sigma, \ell\rangle$ and $|\sigma', \ell'\rangle$, respectively. The superposition state, $|\sigma, \ell, \sigma', \ell'; \alpha, \beta\rangle$, with $\beta \neq 0$ or π is represented by points located on the sphere surface in be-

tween the poles. In this manner, the maximal superposition state is positioned at the equator ($\beta = \pi/2$), in contrast to the north/south pole, which no longer signifies a VVB but instead represents an individual TL state.

The vector potential of such a VVB is given by $\mathcal{A}^{\sigma,\ell,-\sigma,\ell'}(\mathbf{q}_{\parallel}; \alpha, \beta) = \cos(\beta/2)\mathcal{A}^{\sigma,\ell}(\mathbf{q}_{\parallel}) + e^{i\alpha}\sin(\beta/2)\mathcal{A}^{-\sigma,\ell'}(\mathbf{q}_{\parallel})$ and leads to the corresponding complex optical matrix element for an exciton in the state $|S, \mathbf{Q}\rangle$, $\tilde{M}_{S,\mathbf{Q}}^{\sigma,\ell,-\sigma,\ell'}(\alpha, \beta) = \cos(\beta/2)\tilde{M}_{S,\mathbf{Q}}^{\sigma,\ell} + e^{i\alpha}\sin(\beta/2)\tilde{M}_{S,\mathbf{Q}}^{-\sigma,\ell'}$. Following Eq. (2), one can show that the squared magnitude of the transverse component of the vector potential in angular spectrum representation is $|\mathcal{A}_{\parallel}^{\sigma,\ell,-\sigma,\ell'}(\mathbf{q}_{\parallel}; \alpha, \beta)|^2 = \cos^2(\beta/2)F_{|\ell|}^2(q_{\parallel}) + \sin^2(\beta/2)F_{|\ell'|}^2(q_{\parallel})$. One notes that the amplitude of the in-plane field of VVB is independent of the azimuthal angle, $\phi_{\mathbf{q}}$. Thus, $|\mathcal{A}_{\parallel}^{\sigma,\ell,-\sigma,\ell'}(\mathbf{q}_{\parallel}; \alpha, \beta)|^2$ exhibits the isotropic contours over the \mathbf{q}_{\parallel} -plane, as shown in Fig. 4(a), and does not preserve the optical information of ℓ carried by the TL basis that is encoded in the phase term, $e^{i\ell\phi_{\mathbf{q}}}$, of Eq. (2).

By contrast, the squared magnitude of the longitudinal component of the vector potential of the same VVB is derived as $|\mathcal{A}_z^{\sigma,\ell,-\sigma,\ell'}(\mathbf{q}_{\parallel}; \alpha, \beta)|^2 = \frac{\sin^2\theta_{\mathbf{q}}}{2}[\cos^2\frac{\beta}{2}F_{|\ell|}^2(q_{\parallel}) + \sin^2\frac{\beta}{2}F_{|\ell'|}^2(q_{\parallel}) + \sin\beta F_{|\ell|}(q_{\parallel})F_{|\ell'|}(q_{\parallel})\cos(\Delta J\phi_{\mathbf{q}} + (\alpha - \frac{\pi}{2}(|\ell'| - |\ell|)))]$ and shown the $\phi_{\mathbf{q}}$ -dependence, as long as $\beta \neq 0, \pi$ and $\Delta J \equiv J' - J = (\sigma' + \ell') - (\sigma + \ell) \neq 0$.

Interestingly, the $\phi_{\mathbf{q}}$ -dependence of $|\mathcal{A}_z^{\sigma,\ell,-\sigma,\ell'}(\mathbf{q}_{\parallel}; \alpha, \beta)|^2$ is featured with the winding number $\Delta J = \ell' - \ell - 2\sigma$ that reflects the difference of TAM between the two TL basis. Figure 4(b) shows the distribution of the squared magnitude of the longitudinal component of the vector potential, $|\mathcal{A}_z^{1,1,-1,-1}(\mathbf{q}_{\parallel}; \alpha, \beta)|^2$, over the \mathbf{q}_{\parallel} -plane for the VVB superposed by the TLs with $(\sigma, \ell) = (1, 1)$ and $(\sigma', \ell') = (-1, -1)$. Indeed, we observe the anisotropic patterns of $|\mathcal{A}_z^{1,1,-1,-1}(\mathbf{q}_{\parallel}; \alpha, \beta = \pi/2)|^2$ in the four-fold rotational symmetry, matching $\Delta J = -4$ of the VVB.

Further, from Eq. (7) one can derive the total transition rate of the spectrally unresolvable BX doublet with \mathbf{Q} under the excitation

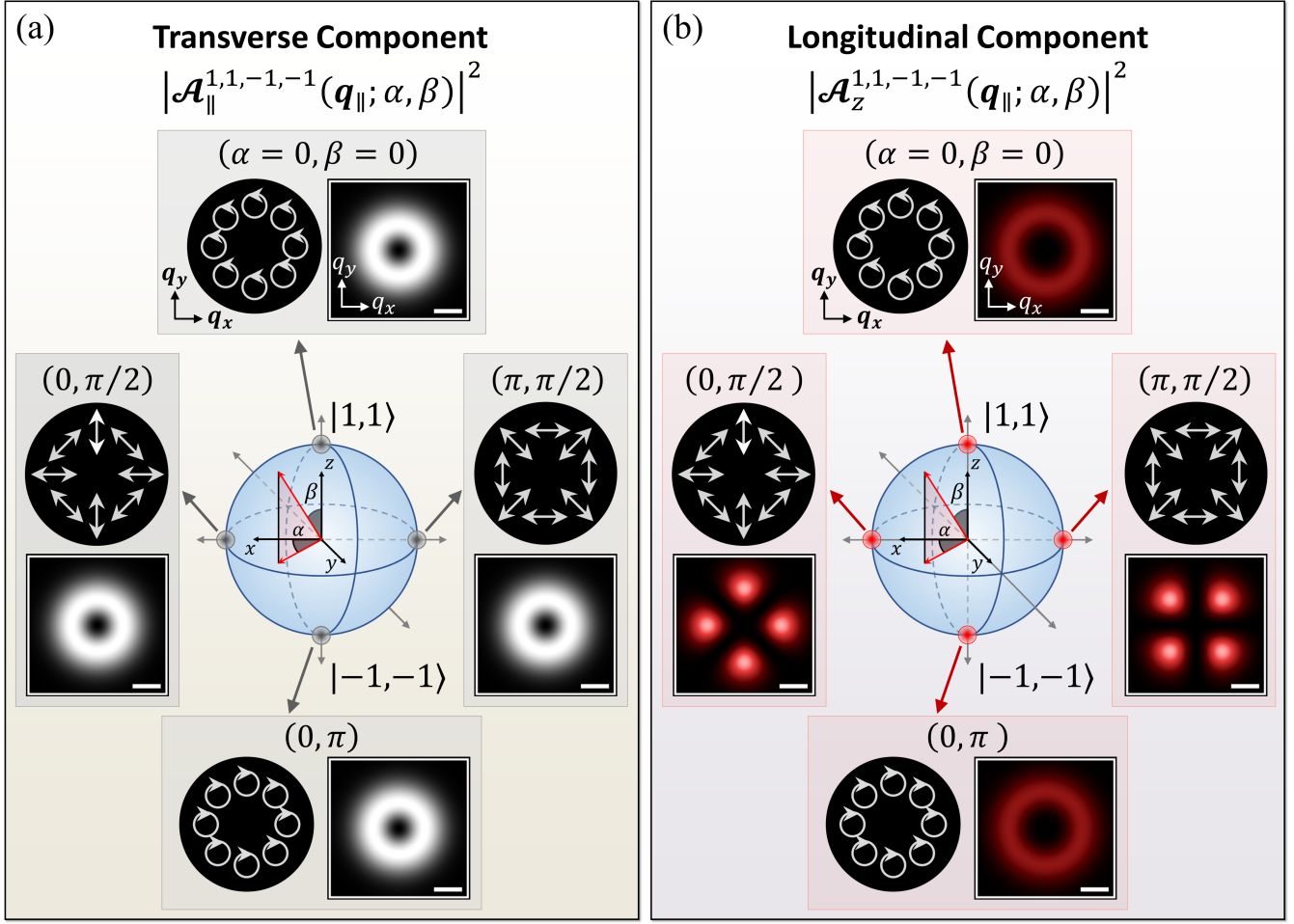


Figure 4: Representation of higher-order Poincaré sphere for the superposition states, $|\sigma, \ell, \sigma', \ell'; \alpha, \beta\rangle$, of VVBs in the basis of the two TLs with $(\sigma = 1, \ell = 1)$ and $(\sigma' = -1, \ell' = -1)$. (a) Density plots of the squared magnitudes of the transverse components of the vector potentials, $|\mathcal{A}_{\parallel}^{1,1,-1,-1}(\mathbf{q}_{\parallel}; \alpha, \beta)|^2$, for the VVB states at the poles and equator of higher-order Poincaré sphere over the \mathbf{q}_{\parallel} -plane. For reference, the length of the horizontal bar in white color represents the magnitude of $q_{\parallel} = 0.1Q_c$. (b) Density plots of the squared magnitudes of the longitudinal components of the vector potentials, $|\mathcal{A}_z^{1,1,-1,-1}(\mathbf{q}_{\parallel}; \alpha, \beta)|^2$, of the same VVBs as presented in (a). While the pattern of $|\mathcal{A}_{\parallel}^{1,1,-1,-1}(\mathbf{q}_{\parallel}; \alpha, \beta)|^2$ always remain isotropic as varying the geometric angles of the superposition states of VVB, those of $|\mathcal{A}_z^{1,1,-1,-1}(\mathbf{q}_{\parallel}; \alpha, \beta = \pi/2)|^2$ of the equatorial superposition states exhibit anisotropic patterns, possessing the rotational symmetry associated with the finite $\ell \neq 0$ carried by the TL basis of the VVB. The dark circular panels in (a) and (b) present the spatially varying transverse polarizations of the VVBs over the \mathbf{q}_{\parallel} -plane. The pure states of TL basis at the poles ($\beta = 0, \pi$) possess circular polarization. By contrast, the maximal superposition states of VVB at the equatorial points ($\beta = \pi/2$), are linearly polarized along the direction depending on \mathbf{q}_{\parallel} .

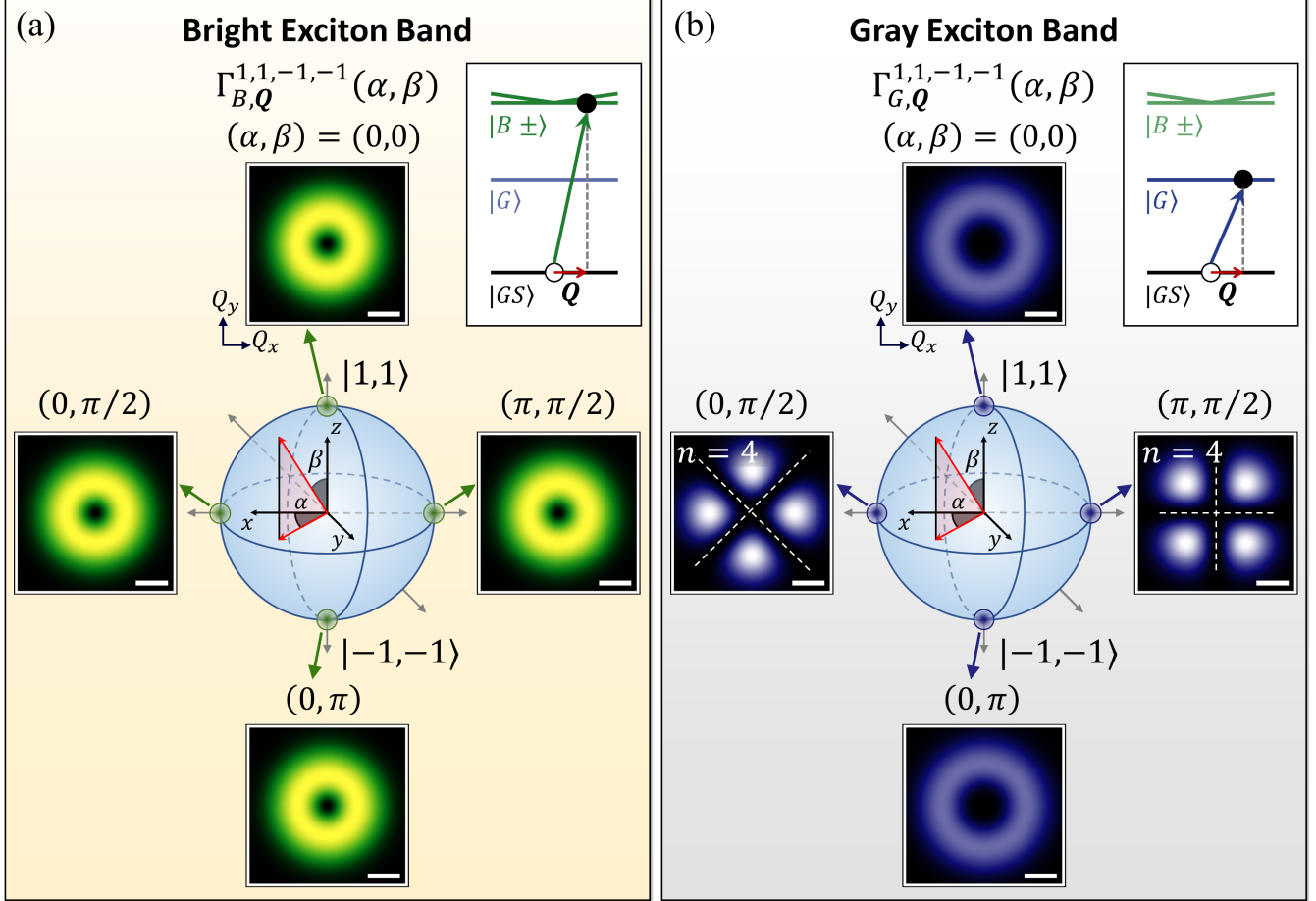


Figure 5: (a) Density plots of the Q -dependent transition rates, $\Gamma_{B,Q}^{1,1,-1,-1}(\alpha, \beta)$, of the finite-momentum BX doublet, $|B\pm, Q\rangle$, and (b) the Q -dependent transition rates, $\Gamma_{G,Q}^{1,1,-1,-1}(\alpha, \beta)$, of the finite-momentum GX state, $|G, Q\rangle$, under the excitation of the VVBs in the TL-superposition states, $|1, 1, -1, -1; \alpha, \beta\rangle$, with the different geometric angles, $(\alpha, \beta) = (0, 0)$, $(0, \pi)$, $(0, \pi/2)$ and $(\pi, \pi/2)$, in the higher order Poincaré sphere representation. The schematic inset in each panel illustrates the optical transition corresponding to each case. For reference, the length of the horizontal bar in white color represents the magnitude of $Q = 0.1Q_c$. Notably, $\Gamma_{G,Q}^{1,1,-1,-1}(\alpha, \beta = \pi/2)$ exhibits the anisotropic patterns with the four-fold rotation symmetry ($n = 4$), from which the angular momentum, ℓ and $\ell' (= -\ell)$, carried by the TL basis can be inferred according to Eq. (10).

of a VVB, $\Gamma_{B,\mathbf{Q}}^{\sigma,\ell,-\sigma,\ell'} \propto \sum_{S=B\pm} |\tilde{M}_{S,\mathbf{Q}}^{\sigma,\ell,-\sigma,\ell'}|^2 = \left[\frac{E_g}{2\hbar} \left(\frac{D_{B+,\mathbf{Q}}^X + D_{B-,\mathbf{Q}}^X}{2} \right) \right]^2 \left[\cos^2 \frac{\beta}{2} F_{|\ell|}^2(Q) + \sin^2 \frac{\beta}{2} F_{|\ell'|}^2(Q) \right]$. As expected, the transition rate of BX doublet, $\Gamma_{B,\mathbf{Q}}^{\sigma,\ell,-\sigma,\ell'}$, excited by a VVB is shown $\phi_{\mathbf{Q}}$ -irrelevant and exhibit an isotropic

$$\Gamma_{G,\mathbf{Q}}^{\sigma,\ell,\sigma',\ell'}(\alpha, \beta) \propto \left(\frac{E_g D_{G,\mathbf{Q}}^X}{2\hbar} \right)^2 \frac{\sin^2 \theta_{\mathbf{Q}}}{2} \left[\cos^2 \frac{\beta}{2} F_{|\ell|}^2(Q) + \sin^2 \frac{\beta}{2} F_{|\ell'|}^2(Q) + F_{|\ell|}(Q) F_{|\ell'|}(Q) \sin \beta \cos(\Delta J \phi_{\mathbf{Q}} + (\alpha - \Delta|\ell|\frac{\pi}{2})) \right], \quad (9)$$

where $\Delta|\ell| \equiv |\ell'| - |\ell|$. The first two terms in Eq. (9) can be viewed as the sum of the squared magnitude of the transition rate of GX under the excitation of the two non-interfered TL-basis of the VVB, which depends only on the magnitude of \mathbf{Q} and remains invariant with varying $\phi_{\mathbf{Q}}$. The last cross-term arises from the coherent interference between the two TL basis and explicitly shows the $\phi_{\mathbf{Q}}$ -dependence, which is importantly associated with the difference of TAM between the TL basis, ΔJ . As $(\alpha - \Delta|\ell|\pi/2)$ is simply a constant phase, the last cross-term of Eq. (9), $\propto \cos(\Delta J \phi_{\mathbf{Q}} + (\alpha - \Delta|\ell|\frac{\pi}{2}))$, varies sinusoidally with the winding number, i.e. $n = |\Delta J|$, by rotating $\phi_{\mathbf{Q}}$.

This suggests that one can decode the angular momentum difference (ΔJ) within the VVB by analyzing the angle-dependent optical spectrum of a GX under the photo-excitation of VVB, which is associated with the \mathbf{Q} -dependence of $\Gamma_{G,\mathbf{Q}}^{\sigma,\ell,\sigma',\ell'}$,⁷⁰ thereby inferring the optically transferred TAM in the excited GX state. The effect made by the last cross-term of Eq. (9) is especially pronounced as the functional product of $F_{|\ell|}(Q)F_{|\ell'|}(Q)$ and the factor $\sin \beta$ is significantly valued. The two form factors are maximized as $\ell = -\ell'$ and $\beta = \pi/2$. For a VVB with $\ell = -\ell'$ and $\sigma = -\sigma'$, the winding number for the cross term, $n = |\Delta J| = |\ell' + \sigma' - \ell - \sigma| = 2|\ell + \sigma|$. Figure 5(a) shows the squared magnitudes of the transition rates, $\Gamma_{B,\mathbf{Q}}^{+1,1,-1,-1}(\alpha, \beta)$, of the BX doublet under the excitation of the VVBs formed by the superposition of the TLs, $|1, 1\rangle$ and $|-1, -1\rangle$, with the different geometric angles, $(\alpha, \beta) = (0, 0)$, $(0, \pi)$, $(0, \pi/2)$ and $(\pi, \pi/2)$. The four selected

distribution over the \mathbf{Q} -plane, as shown by Fig. 5(a) for the VVB with $(\sigma, \ell) = (1, 1)$ and $(\sigma', \ell') = (-1, -1)$. For a GX, the transition rate, $\Gamma_{G,\mathbf{Q}}^{\sigma,\ell,\sigma',\ell'}(\alpha, \beta) \propto |M_{G,\mathbf{Q}}^{\sigma,\ell,\sigma',\ell'}(\alpha, \beta)|^2$, is derived as

VVBs are indicated by the north pole, south pole, and the two positions at the equator of the high-order Poincaré sphere. Under the excitation of the same VVBs, Figure 5(b) shows the squared magnitudes of the \mathbf{Q} -dependent transition rates, $\Gamma_{G,\mathbf{Q}}^{+1,1,-1,-1}$, for the GX states.

As expected from the preceding analysis, the donut-like distribution of the $\Gamma_{B,\mathbf{Q}}^{+1,1,-1,-1}(\alpha, \beta)$ over the \mathbf{Q} -space for the BX doublet under the excitation of the superposition TLs remains invariant against the varied α and β (see Supporting Information). By contrast, the distribution of the $\Gamma_{G,\mathbf{Q}}^{+1,1,-1,-1}(\alpha, \beta)$ over the \mathbf{Q} -plane for the GX states varies with changing the geometric angles, α and β . In particular, at the equator ($\beta = \pi/2$) where the VVB is the maximal superposition of TLs, the $\phi_{\mathbf{Q}}$ -varying patterns of $\Gamma_{G,\mathbf{Q}}^{+1,1,-1,-1}(\alpha, \pi/2)$, exhibits the anisotropic patterns with the four-fold ($n = 4$) rotation symmetry that directly reflect $|\Delta J| = 4$ carried by the incident VVB. Generalizing the analysis for the TLs carrying arbitrary OAM, one can show that the transferred OAM to a GX can be inferred from the n -fold pattern of $\Gamma_{G,\mathbf{Q}}^{+1,\ell,-1,-\ell}(0, \pi/2)$ according to the formulation,

$$|\ell| = (n - 2)/2. \quad (10)$$

The calculated \mathbf{Q} -dependent patterns of $\Gamma_{G,\mathbf{Q}}^{+1,\ell,-1,-\ell}(0, \pi/2)$ for the GX states excited by the VVBs in the higher order modes with $\ell = 2, 3, 4$ are presented in Fig. S4 of Supporting Information, confirming the formalism for extracting the transferred angular momentum from the n -fold rotational symmetry of the \mathbf{Q} -dependent pattern of the magnitudes of the transition rates of the GXs by VVBs. Note

that, in this manner, the optical information of OAM is imprinted in the n -fold petal-like pattern of the squared magnitude of the transition rates of GXs over the \mathbf{Q} -plane, which is measurable by the angle-resolved optical spectroscopy, with no need of good coherence in materials.

Read-Out of Imprinted OAM: Angle-Resolved Optical Spectroscopy

The momentum-dependent transition rates presented in Fig. 5 can be related to the angle-dependent optical pattern.⁸⁴ Accordingly, the feasibility of using the angle-resolved optical spectroscopy^{70,84,96,116} to infer the imprinted optical information in the GXs photo-generated by a VVB is suggested.

Following the theory of Section III.B in Ref. (84), the angle-dependent transition rate of the light emission from an BX and GX state is derived as

$$\Gamma_B(\theta_\nu, \phi_\nu) \propto \left| \tilde{M}_{B^+, \mathbf{Q}}^{\sigma, \ell} \right|^2 \left| D_{B^+, \mathbf{Q}}^X \right|^2 \left[1 - \left(\frac{Q}{Q_c} \right)^2 \right] + \left| \tilde{M}_{B^-, \mathbf{Q}}^{\sigma, \ell} \right|^2 \left| D_{B^-, \mathbf{Q}}^X \right|^2 \quad (11)$$

and

$$\Gamma_G(\theta_\nu, \phi_\nu) \propto \left| \tilde{M}_{G, \mathbf{Q}}^{\sigma, \ell} \right|^2 \left| D_{G, \mathbf{Q}}^X \right|^2 \left(\frac{Q}{Q'_c} \right)^2, \quad (12)$$

respectively, where θ_ν and ϕ_ν are the polar and azimuthal angles of the emitted plane-wave light, respectively. In the equations, the angles, θ_ν and ϕ_ν , of emitted light are related to the vectorial momentum of exciton, $\mathbf{Q} = Q(\cos \phi_{\mathbf{Q}} \hat{\mathbf{x}} + \sin \phi_{\mathbf{Q}} \hat{\mathbf{y}})$, following the conservation laws of momentum and energy. The momentum conservation law ensures that $\phi_\nu = \phi_{\mathbf{Q}}$, while the energy conservation law leads to $\theta_\nu = \sin^{-1}(Q/Q_c)$, where $Q_c = E_{S,0}^X/\hbar c$ is the light-cone radius. Because of the different energies, the wavevectors of light-cone edges for a BX and GX slightly differ, which are given by $Q_c = E_{B^\pm,0}^X/\hbar c$ and $Q'_c = E_{G,0}^X/\hbar c \approx Q_c$, respectively.

In Fig. 6, we show the angle-dependent optical transition rates of the BX doublet and GX state excited by the ℓ -encoded VVBs, $|\sigma, \ell, -\sigma, -\ell; \alpha, \beta\rangle$, with different values of ℓ . Apparently, one sees that the azimuthal-angle-dependence of the transition rate of the GX state reflect the n -fold rotation symmetry of the squared magnitude of the transition rate of the GX state photo-excited by the VVB in the equator state presented in Fig. 5(b). As the transition dipoles of GXs are weakly \mathbf{Q} -dependence, according to Eq. (12), the azimuthal-angle-dependence of the optical pattern of an GX mainly follow the $\phi_{\mathbf{Q}}$ -dependence of the transition rate. Hence, it is suggested to read out the imprinted optical information in VVB-excited GX states by analyzing the azimuthal-angle-dependences of the optical patterns that are measurable by angle-resolved optical spectroscopy.^{70,84,96,116}

CONCLUSION

In summary, we have presented a comprehensive investigation based on first-principles, focusing on the light-matter interaction between structured lights carrying optical angular momenta and tightly bound excitons in 2D materials. We show that the photo-excitation of a specific type of spin-forbidden dark excitons, i.e. gray exciton, is greatly enhanced by the incident twisted lights that carry orbital angular momentum and possess the longitudinal field component associated with the interaction between spin and orbital angular momenta. Moreover, we investigate the superposition of two twisted lights with distinct SAM and OAM, resulting in the formation of a vector vortex beam (VVB) that is spatially engineered in both complex amplitude and polarization as well. Our research demonstrates that a spin-orbit-coupled VVB in a non-separable form surprisingly allows for the imprinting of the carried optical information onto gray excitons in 2D materials, which is robust against the decoherence mechanisms in materials. These studies unveil the indispensable role of gray excitons in twisted-light-based optoelectronics and suggest the uti-

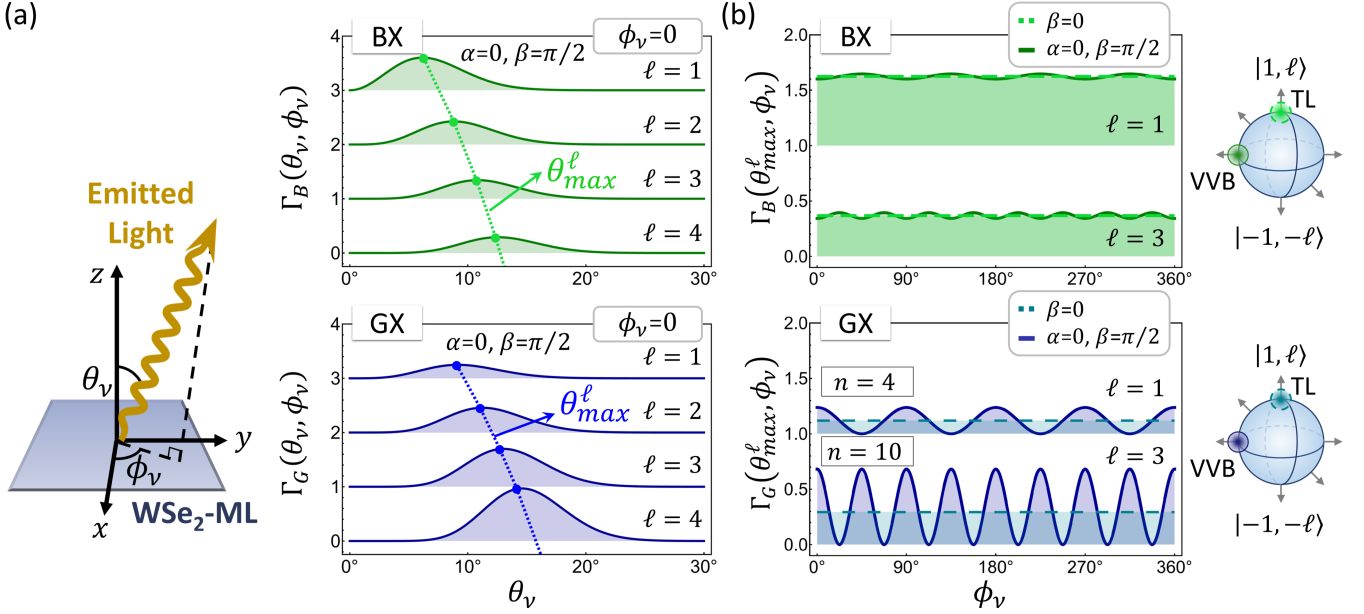


Figure 6: The angle-dependent optical transition rate, $\Gamma_S(\theta_\nu, \phi_\nu)$, of the BX doublet and GX states excited by the ℓ -encoded VVB and single TL. (a) The θ_ν -dependence of the transition rate, $\Gamma_S(\theta_\nu, \phi_\nu = 0)$, for the BX (upper) and GX states (lower) photo-excited by the ℓ -encoded VVB state $|\sigma, \ell, -\sigma, -\ell; \alpha, \beta\rangle$ along the x - z plane ($\phi_\nu = 0$). Note that the polar angle, θ_{max}^ℓ , for the maximum transition rate increases with the increasing value of ℓ in the VVB. The schematic on the left-hand side illustrates the polar, θ_ν , and azimuthal angle, ϕ_ν , of the light emitted from a WSe₂-ML. (b) The ϕ_ν -dependence of the transition rate, $\Gamma_S(\theta_\nu = \theta_{max}^\ell, \phi_\nu)$, for the BX (upper) and GX states (lower) excited by the ℓ -encoded single TL (i.e. the state with $\beta = 0$ on the Poincaré sphere) and VVB with $(\alpha = 0, \beta = \pi/2)$ at $\theta_\nu = \theta_{max}^\ell$. Note that the ϕ_ν -dependence of the transition rate of the GX states mainly follow the n -fold patterns appeared in the ϕ_Q -dependence of the transition rates in Fig. 5(b).

lization of VVB for transferring optical information onto 2D materials.

METHODS

Density Functional Theory calculations.

The Density Functional Theory (DFT) calculations were conducted using the PBE functional¹¹⁷ as implemented in the Quantum Espresso software package.¹¹⁸ The supercell was constructed with a 30 Å-high vacuum in the aperiodic direction and an in-plane lattice constant of 3.35 Å. A plane-wave cutoff energy of 1632 eV was employed for the expansion of wavefunctions, along with norm-conserving pseudo-potentials. The electronic structure calculations utilized a Monkhorst-Pack grid of $9 \times 9 \times 1$ points to sample the first Brillouin zone. Convergence of the electronic self-consistent loop was achieved with a break condition set to 1.36×10^{-9} eV.

ASSOCIATED CONTENT

Supporting Information

Technical details on establishing the Bethe-Salpeter equation based on first-principles; guidelines for evaluating the transition dipole of an exciton; formalisms for Laguerre-Gaussian beams in both real and momentum space under the Coulomb gauge; demonstration of the encoding of various angular momentum in the transition rates of gray excitons.

ACKNOWLEDGMENTS

This study is supported by National Science and Technology Council of Taiwan, under contracts, MOST 109-2112 -M-009 -018 -MY3.

References

(1) Couillet, P.; Gil, L.; Rocca, F. Optical Vortices. Opt. Commun. **1989**, 73, 403–408.

- (2) Allen, L.; Beijersbergen, M. W.; Spreeuw, R. J. C.; Woerdman, J. P. Orbital Angular Momentum of Light and the Transformation of Laguerre-Gaussian Laser Modes. Phys. Rev. A **1992**, 45, 8185–8189.
- (3) Courtial, J.; Dholakia, K.; Robertson, D. A.; Allen, L.; Padgett, M. J. Measurement of the Rotational Frequency Shift Imparted to a Rotating Light Beam Possessing Orbital Angular Momentum. Phys. Rev. Lett. **1998**, 80, 3217–3219.
- (4) O’Neil, A. T.; MacVicar, I.; Allen, L.; Padgett, M. J. Intrinsic and Extrinsic Nature of the Orbital Angular Momentum of a Light Beam. Phys. Rev. Lett. **2002**, 88, 053601.
- (5) Padgett, M.; Bowman, R. Tweezers with a Twist. Nat. Photonics **2011**, 5, 343–348.
- (6) Gong, L.; Gu, B.; Rui, G.; Cui, Y.; Zhu, Z.; Zhan, Q. Optical Forces of Focused Femtosecond Faser Pulses on Nonlinear Optical Rayleigh Particles. Photonics Res. **2018**, 6, 138–143.
- (7) Otte, E.; Denz, C. Optical Trapping Gets Structure: Structured Light for Advanced Optical Manipulation. Appl. Phys. Rev. **2020**, 7, 041308.
- (8) Yang, Y.; Ren, Y.-X.; Chen, M.; Arita, Y.; Rosales-Guzmán, C. Optical Trapping with Structured Light: a Review. Adv. Photonics **2021**, 3, 034001.
- (9) Tan, P.; Yuan, X.-C.; Yuan, G.; Wang, Q. High-Resolution Wide-Field Standing-Wave Surface Plasmon Resonance Fluorescence Microscopy with Optical Vortices. Appl. Phys. Lett. **2010**, 97, 241109.
- (10) Zhang, C.; Min, C.; Du, L.; Yuan, X.-C. Perfect Optical Vortex Enhanced Surface Plasmon Excitation for Plasmonic Structured Illumination Microscopy Imaging. Appl. Phys. Lett. **2016**, 108, 201601.

- (11) Ritsch-Martel, M. Orbital Angular Momentum Light in Microscopy. Philos. Trans. R. Soc. A **2017**, 375, 20150437.
- (12) Wang, J.; Yang, J.-Y.; Fazal, I. M.; Ahmed, N.; Yan, Y.; Huang, H.; Ren, Y.; Yue, Y.; Dolinar, S.; Tur, M.; Willner, A. E. Terabit Free-Space Data Transmission Employing Orbital Angular Momentum Multiplexing. Nat. Photonics **2012**, 6, 488–496.
- (13) Xie, Z.; Lei, T.; Li, F.; Qiu, H.; Zhang, Z.; Wang, H.; Min, C.; Du, L.; Li, Z.; Yuan, X. Ultra-Broadband on-Chip Twisted Light Emitter for Optical Communications. Light Sci. Appl. **2018**, 7, 18001.
- (14) Mair, A.; Vaziri, A.; Weihs, G.; Zeilinger, A. Entanglement of the Orbital Angular Momentum States of Photons. Nature **2001**, 412, 313–316.
- (15) Fickler, R.; Lapkiewicz, R.; Plick, W. N.; Krenn, M.; Schaeff, C.; Ramelow, S.; Zeilinger, A. Quantum Entanglement of High Angular Momenta. Science **2012**, 338, 640–643.
- (16) Al-Amri, M.; El-Gomati, M.; Zubairy, M. Optics in Our Time; Springer International Publishing, 2016; Chapter 17, pp 435–454.
- (17) Erhard, M.; Fickler, R.; Krenn, M.; Zeilinger, A. Twisted Photons: New Quantum Perspectives in High Dimensions. Light Sci. Appl. **2018**, 7, 17146.
- (18) Allen, L.; Lembessis, V. E.; Babiker, M. Spin-Orbit Coupling in Free-Space Laguerre-Gaussian Light Beams. Phys. Rev. A **1996**, 53, R2937–R2939.
- (19) Eismann, J. S.; Banzer, P.; Neugebauer, M. Spin-Orbit Coupling Affecting the Evolution of Transverse Spin. Phys. Rev. Res. **2019**, 1, 033143.
- (20) Bliokh, K. Y.; Rodríguez-Fortuño, F. J.; Nori, F.; Zayats, A. V. Spin-Orbit Interactions of Light. Nat. Photonics **2015**, 9, 796–808.
- (21) Bliokh, K. Y.; Smirnova, D.; Nori, F. Quantum Spin Hall Effect of Light. Science **2015**, 348, 1448–1451.
- (22) Ling, X.; Zhou, X.; Huang, K.; Liu, Y.; Qiu, C.-W.; Luo, H.; Wen, S. Recent Advances in the spin Hall Effect of Light. Rep. Prog. Phys. **2017**, 80, 066401.
- (23) Bahari, B.; Hsu, L.; Pan, S. H.; Preece, D.; Ndao, A.; El Amili, A.; Fainman, Y.; Kanté, B. Photonic Quantum Hall Effect and Multiplexed Light Sources of Large Orbital Angular Momenta. Nat. Phys. **2021**, 17, 700–703.
- (24) Kim, M.; Yang, Y.; Lee, D.; Kim, Y.; Kim, H.; Rho, J. Spin Hall Effect of Light: From Fundamentals to Recent Advancements. Laser Photonics Rev. **2023**, 17, 2200046.
- (25) Yu, X.; Wang, X.; Li, Z.; Zhao, L.; Zhou, F.; Qu, J.; Song, J. Spin Hall Effect of Light Based on a Surface Plasmonic Platform. Nanophotonics **2021**, 10, 3031–3048.
- (26) Banzer, P.; Neugebauer, M.; Aiello, A.; Marquardt, C.; Lindlein, N.; Bauer, T.; Leuchs, G. The Photonic Wheel-Demonstration of a State of Light with Purely Transverse Angular Momentum. J. Eur. Opt. Soc.: Rapid Publ. **2013**, 8, 13032.
- (27) Aiello, A.; Banzer, P.; Neugebauer, M.; Leuchs, G. From Transverse Angular Momentum to Photonic Wheels. Nat. Photonics **2015**, 9, 789–795.
- (28) Shao, Z.; Zhu, J.; Chen, Y.; Zhang, Y.; Yu, S. Spin-Orbit Interaction of Light Induced by Transverse Spin Angular Momentum Engineering. Nat. Commun. **2018**, 9, 926.

- (29) Zhao, Y.; Edgar, J. S.; Jeffries, G. D. M.; McGloin, D.; Chiu, D. T. Spin-to-Orbital Angular Momentum Conversion in a Strongly Focused Optical Beam. Phys. Rev. Lett. **2007**, 99, 073901.
- (30) Bliokh, K. Y.; Nori, F. Transverse and Longitudinal Angular Momenta of Light. Phys. Rep. **2015**, 592, 1–38.
- (31) Shi, P.; Du, L.; Yuan, X. Structured Spin Angular Momentum in Highly Focused Cylindrical Vector Vortex Beams for Optical Manipulation. Opt. Express **2018**, 26, 23449–23459.
- (32) Forbes, K. A.; Andrews, D. L. Orbital Angular Momentum of Twisted Light: Chirality and Optical Activity. J. Phys. Photonics **2021**, 3, 022007.
- (33) Forbes, K. A.; Green, D.; Jones, G. A. Relevance of Longitudinal Fields of Paraxial Optical Vortices. J. Opt. **2021**, 23, 075401.
- (34) Milione, G.; Sztul, H. I.; Nolan, D. A.; Alfano, R. R. Higher-Order Poincaré Sphere, Stokes Parameters, and the Angular Momentum of Light. Phys. Rev. Lett. **2011**, 107, 053601.
- (35) Naidoo, D.; Roux, F. S.; Dudley, A.; Litvin, I.; Piccirillo, B.; Marrucci, L.; Forbes, A. Controlled Generation of Higher-Order Poincaré Sphere Beams from a Laser. Nat. Photonics **2016**, 10, 327–332.
- (36) Liu, Z.; Liu, Y.; Ke, Y.; Liu, Y.; Shu, W.; Luo, H.; Wen, S. Generation of Arbitrary Vector Vortex Beams on Hybrid-Order Poincaré Sphere. Photonics Res. **2017**, 5, 15–21.
- (37) Huang, T. D.; Lu, T. H. Partial Poincaré Beams Generated from Wavelength-Mismatched Vortex Plates. Opt. Express **2017**, 25, 33184–33192.
- (38) McLaren, M.; Konrad, T.; Forbes, A. Measuring the Nonseparability of Vector Vortex Beams. Phys. Rev. A **2015**, 92, 023833.
- (39) Forbes, A.; de Oliveira, M.; Dennis, M. R. Structured Light. Nat. Photonics **2021**, 15, 253–262.
- (40) Lu, T. H.; Wang, Y. J.; Chen, Y. F.; Lin, Y. H. Generation of Vector Vortex Beams by Axially Symmetric Sheared Polymer Network Liquid Crystals. Opt. Lett. **2022**, 47, 6373–6376.
- (41) Zhang, B.; Chen, Z.; Sun, H.; Xia, J.; Ding, J. Vectorial Optical Vortex Filtering for Edge Enhancement. J. Opt. **2016**, 18, 035703.
- (42) Wong, L. J.; Kärtner, F. X. Direct Acceleration of an Electron in Infinite Vacuum by a Pulsed Radially-Polarized Laser Beam. Opt. Express **2010**, 18, 25035–25051.
- (43) Chen, R.-P.; Chen, Z.; Chew, K.-H.; Li, P.-G.; Yu, Z.; Ding, J.; He, S. Structured Caustic Vector Vortex Optical Field: Manipulating Optical Angular Momentum Flux and Polarization Rotation. Sci. Rep. **2015**, 5, 10628.
- (44) Milione, G.; Lavery, M. P. J.; Huang, H.; Ren, Y.; Xie, G.; Nguyen, T. A.; Karimi, E.; Marrucci, L.; Nolan, D. A.; Alfano, R. R.; Willner, A. E. 4× 20 Gbit/s Mode Division Multiplexing Over Free Space Using Vector Modes and a q-plate Mode (de) Multiplexer. Opt. Lett. **2015**, 40, 1980–1983.
- (45) Fang, J.; Xie, Z.; Lei, T.; Min, C.; Du, L.; Li, Z.; Yuan, X. Spin-Dependent Optical Geometric Transformation for Cylindrical Vector Beam Multiplexing Communication. ACS Photonics **2018**, 5, 3478–3484.
- (46) Tang, J.; Ming, Y.; Chen, Z.-x.; Hu, W.; Xu, F.; Lu, Y.-q. Entanglement of Photons with Complex Spatial Structure in Hermite-Laguerre-Gaussian Modes. Phys. Rev. A **2016**, 94, 012313.

- (47) Krenn, M.; Malik, M.; Erhard, M.; Zeilinger, A. Orbital Angular Momentum of Photons and the Entanglement of Laguerre-Gaussian Modes. Philos. Trans. R. Soc. A **2017**, 375, 20150442.
- (48) Slussarenko, S.; Joch, D. J.; Tischler, N.; Ghafari, F.; Shalm, L. K.; Verma, V. B.; Nam, S. W.; Pryde, G. J. Quantum Steering with Vector Vortex Photon States with the Detection Loophole Closed. npj Quantum Inf. **2022**, 8, 20.
- (49) Quinteiro Rosen, G. F.; Tamborenea, P. I.; Kuhn, T. Interplay Between Optical Vortices and Condensed Matter. Rev. Mod. Phys. **2022**, 94, 035003.
- (50) Simbulan, K. B.; Huang, T.-D.; Peng, G.-H.; Li, F.; Gomez Sanchez, O. J.; Lin, J.-D.; Lu, C.-I.; Yang, C.-S.; Qi, J.; Cheng, S.-J.; Lu, T.-H.; Lan, Y.-W. Selective Photoexcitation of Finite-Momentum Excitons in Monolayer MoS₂ by Twisted Light. ACS Nano **2021**, 15, 3481–3489.
- (51) Ji, Z.; Liu, W.; Krylyuk, S.; Fan, X.; Zhang, Z.; Pan, A.; Feng, L.; Davydov, A.; Agarwal, R. Photocurrent Detection of the Orbital Angular Momentum of Light. Science **2020**, 368, 763–767.
- (52) Session, D.; Mehrabad, M. J.; Paithanker, N.; Grass, T.; Eckhardt, C.; Cao, B.; Forero, D. G. S.; Li, K.; Alam, M. S.; Solomon, G. S.; Schine, N.; Jay, S.; Sordan, R.; Hafezi, M. Optical pumping of electronic quantum Hall states with vortex light. arXiv preprint **2023-06-06**, accessed 2023-08-31.
- (53) Feng, Y.-J.; Simbulan, K. B.; Yang, T. H.; Chen, Y.-R.; Li, K.-S.; Chu, C.-J.; Lu, T.-H.; Lan, Y.-W. Twisted Light-Induced Photocurrent in a Silicon Nanowire Field-Effect Transistor. ACS Nano **2022**, 16, 9297–9303.
- (54) Mak, K. F.; Lee, C.; Hone, J.; Shan, J.; Heinz, T. F. Atomically Thin MoS₂: A New Direct-Gap Semiconductor. Phys. Rev. Lett. **2010**, 105, 136805.
- (55) Bernardi, M.; Palummo, M.; Grossman, J. C. Extraordinary Sunlight Absorption and One Nanometer Thick Photovoltaics Using Two-Dimensional Monolayer Materials. Nano Lett. **2013**, 13, 3664–3670.
- (56) Chernikov, A.; Berkelbach, T. C.; Hill, H. M.; Rigosi, A.; Li, Y.; Aslan, B.; Reichman, D. R.; Hybertsen, M. S.; Heinz, T. F. Exciton Binding Energy and Nonhydrogenic Rydberg Series in Monolayer WS₂. Phys. Rev. Lett. **2014**, 113, 076802.
- (57) He, K.; Kumar, N.; Zhao, L.; Wang, Z.; Mak, K. F.; Zhao, H.; Shan, J. Tightly Bound Excitons in Monolayer WSe₂. Phys. Rev. Lett. **2014**, 113, 026803.
- (58) Manzeli, S.; Ovchinnikov, D.; Pasquier, D.; Yazyev, O. V.; Kis, A. 2D Transition Metal Dichalcogenides. Nat. Rev. Mater. **2017**, 2, 1–15.
- (59) Yu, T.; Wu, M. W. Valley Depolarization Due to Intervalley and Intravalley Electron-Hole Exchange Interactions in Monolayer MoS₂. Phys. Rev. B **2014**, 89, 205303.
- (60) Sauer, M. O.; Nielsen, C. E. M.; Merring-Mikkelsen, L.; Pedersen, T. G. Optical Emission from Light-Like and Particle-Like Excitons in Monolayer Transition Metal Dichalcogenides. Phys. Rev. B **2021**, 103, 205404.
- (61) Lo, P.-Y.; Peng, G.-H.; Li, W.-H.; Yang, Y.; Cheng, S.-J. Full-Zone Valley Polarization Landscape of Finite-Momentum Exciton in Transition Metal Dichalcogenide Monolayers. Phys. Rev. Res. **2021**, 3, 043198.
- (62) Ma, X.; Kudtarkar, K.; Chen, Y.; Cunha, P.; Ma, Y.; Watanabe, K.; Taniguchi, T.; Qian, X.; Hipwell, M. C.;

- Wong, Z. J.; Lan, S. Coherent Momentum Control of Forbidden Excitons. Nat. Commun. **2022**, 13, 6916.
- (63) Li, W.-H.; Lin, J.-D.; Lo, P.-Y.; Peng, G.-H.; Hei, C.-Y.; Chen, S.-Y.; Cheng, S.-J. The Key Role of Non-Local Screening in the Environment-Insensitive Exciton Fine Structures of Transition-Metal Dichalcogenide Monolayers. Nanomaterials **2023**, 13, 1739.
- (64) Chen, S.-Y.; Goldstein, T.; Taniguchi, T.; Watanabe, K.; Yan, J. Coulomb-Bound Four-and Five-Particle Intervalley States in an Atomically-Thin Semiconductor. Nat. Commun. **2018**, 9, 3717.
- (65) Molas, M. R.; Faugeras, C.; Slobodeniuk, A. O.; Nogajewski, K.; Bartos, M.; Basko, D.; Potemski, M. Brightening of Dark Excitons in Monolayers of Semiconducting Transition Metal Dichalcogenides. 2D Mater. **2017**, 4, 021003.
- (66) Zinkiewicz, M.; Slobodeniuk, A.; Kazimierzczuk, T.; Kapuściński, P.; Oreszczuk, K.; Grzeszczyk, M.; Bartos, M.; Nogajewski, K.; Watanabe, K.; Taniguchi, T.; others Neutral and charged dark excitons in monolayer WS₂. Nanoscale **2020**, 12, 18153–18159.
- (67) Wang, G.; Robert, C.; Glazov, M. M.; Cadiz, F.; Courtade, E.; Amand, T.; Lagarde, D.; Taniguchi, T.; Watanabe, K.; Urbaszek, B.; Marie, X. In-Plane Propagation of Light in Transition Metal Dichalcogenide Monolayers: Optical Selection Rules. Phys. Rev. Lett. **2017**, 119, 047401.
- (68) Robert, C.; Amand, T.; Cadiz, F.; Lagarde, D.; Courtade, E.; Manca, M.; Taniguchi, T.; Watanabe, K.; Urbaszek, B.; Marie, X. Fine Structure and Lifetime of Dark Excitons in Transition Metal Dichalcogenide Monolayers. Phys. Rev. B **2017**, 96, 155423.
- (69) Robert, C.; Han, B.; Kapuscinski, P.; Delhomme, A.; Faugeras, C.; Amand, T.; Molas, M. R.; Bartos, M.; Watanabe, K.; Taniguchi, T.; Urbaszek, B.; Potemski, M.; Marie, X. Measurement of the Spin-Forbidden Dark Excitons in MoS₂ and MoSe₂ Monolayers. Nat. Commun. **2020**, 11, 4037.
- (70) Schneider, L. M.; Esdaille, S. S.; Rhodes, D. A.; Barmak, K.; Hone, J. C.; Rahimi-Iman, A. Direct Measurement of the Radiative Pattern of Bright and Dark Excitons and Exciton Complexes in Encapsulated Tungsten Diselenide. Sci. Rep. **2020**, 10, 8091.
- (71) Feierabend, M.; Berghäuser, G.; Knorr, A.; Malic, E. Proposal for Dark Exciton Based Chemical Sensors. Nat. Commun. **2017**, 8, 14776.
- (72) Jiang, C.; Xu, W.; Rasmita, A.; Huang, Z.; Li, K.; Xiong, Q.; Gao, W.-b. Microsecond Dark-Exciton Valley Polarization Memory in Two-Dimensional Heterostructures. Nat. Commun. **2018**, 9, 753.
- (73) Zhang, X.-X.; Cao, T.; Lu, Z.; Lin, Y.-C.; Zhang, F.; Wang, Y.; Li, Z.; Hone, J. C.; Robinson, J. A.; Smirnov, D.; Louie, S. G.; Heinz, T. F. Magnetic Brightening and Control of Dark Excitons in Monolayer WSe₂. Nat. Nanotechnol. **2017**, 12, 883–888.
- (74) Zhou, Y.; Scuri, G.; Wild, D. S.; High, A. A.; Dibos, A.; Jauregui, L. A.; Shu, C.; De Greve, K.; Pistunova, K.; Joe, A. Y.; Taniguchi, T.; Watanabe, K.; Kim, P.; Lukin, M. D.; Park, H. Probing Dark Excitons in Atomically Thin Semiconductors Via Near-Field Coupling to Surface Plasmon Polaritons. Nat. Nanotechnol. **2017**, 12, 856–860.
- (75) Tang, Y.; Mak, K. F.; Shan, J. Long Valley Lifetime of Dark Excitons in Single-Layer WSe₂. Nat. Commun. **2019**, 10, 4047.

- (76) Luo, Y.; Liu, N.; Kim, B.; Hone, J.; Strauf, S. Exciton dipole orientation of strain-induced quantum emitters in WSe₂. Nano Lett. **2020**, 20, 5119–5126.
- (77) Li, Z.; Wang, T.; Lu, Z.; Khatoniar, M.; Lian, Z.; Meng, Y.; Blei, M.; Taniguchi, T.; Watanabe, K.; McGill, S. A.; others Direct observation of gate-tunable dark trions in monolayer WSe₂. Nano Lett. **2019**, 19, 6886–6893.
- (78) Shigematsu, K.; Toda, Y.; Yamane, K.; Morita, R. Orbital Angular Momentum Spectral Dynamics of GaN Excitons Excited by Optical Vortices. Jpn. J. Appl. Phys. **2013**, 52, 08JL08.
- (79) Shigematsu, K.; Yamane, K.; Morita, R.; Toda, Y. Coherent Dynamics of Exciton Orbital Angular Momentum Transferred by Optical Vortex Pulses. Phys. Rev. B **2016**, 93, 045205.
- (80) Yang, H.; Pan, J.; Zhang, S.; Zhu, W.; Zhang, L.; Zheng, H.; Zhong, Y.; Yu, J.; Chen, Z. Steering Nonlinear Twisted Valley Photons of Monolayer WS₂ by Vector Beams. Nano Lett. **2021**, 21, 7261–7269.
- (81) Pattanayak, A. K.; Das, P.; Dhara, A.; Chakrabarty, D.; Paul, S.; Gurnani, K.; Brundavanam, M. M.; Dhara, S. A Steady-State Approach for Studying Valley Relaxation Using an Optical Vortex Beam. Nano Letters **2022**, 22, 4712–4717.
- (82) Graß, T.; Bhattacharya, U.; Sell, J.; Hafezi, M. Two-dimensional excitons from twisted light and the fate of the photon's orbital angular momentum. Phys. Rev. B **2022**, 105, 205202.
- (83) Kesarwani, R.; Simbulan, K. B.; Huang, T.-D.; Chiang, Y.-F.; Yeh, N.-C.; Lan, Y.-W.; Lu, T.-H. Control of Trion-to-Exciton Conversion in Monolayer WS₂ by Orbital Angular Momentum of Light. Sci. Adv. **2022**, 8, eabm0100.
- (84) Peng, G.-H.; Sanchez, O. J. G.; Li, W.-H.; Lo, P.-Y.; Cheng, S.-J. Tailoring the Superposition of Finite-Momentum Valley Exciton States in Transition-Metal Dichalcogenide Monolayers by Using Polarized Twisted Light. Phys. Rev. B **2022**, 106, 155304.
- (85) Zhang, D.; Zhai, D.; Deng, S.; Yao, W.; Zhu, Q. Single Photon Emitters with Polarization and Orbital Angular Momentum Locking in Monolayer Semiconductors. Nano Letters **2023**, 23, 3851–3857.
- (86) Pattanayak, A. K.; Das, P.; Chakrabarty, D.; Dhara, A.; Paul, S.; Maji, S.; Brundavanam, M. M.; Dhara, S. Probing spin dynamics of 2D excitons with twisted light. ACS Photonics **2022**, 9, 3351–3356.
- (87) Quinteiro, G. F.; Schmidt-Kaler, F.; Schmiegelow, C. T. Twisted-Light-Ion Interaction: The Role of Longitudinal Fields. Phys. Rev. Lett. **2017**, 119, 253203.
- (88) Romero, L. D.; Andrews, D.; Babiker, M. A Quantum Electrodynamics Framework for the Nonlinear Optics of Twisted Beams. J. Opt. B: Quantum and Semiclassical Optics **2002**, 4, S66.
- (89) Jones, A. M.; Yu, H.; Ghimire, N. J.; Wu, S.; Aivazian, G.; Ross, J. S.; Zhao, B.; Yan, J.; Mandrus, D. G.; Xiao, D.; Yao, W.; Xu, X. Optical Generation of Excitonic Valley Coherence in Monolayer WSe₂. Nat. Nanotechnol. **2013**, 8, 634–638.
- (90) Huang, J.; Hoang, T. B.; Mikkelsen, M. H. Probing the Origin of Excitonic States in Monolayer WSe₂. Sci. Rep. **2016**, 6, 22414.
- (91) Huang, J.; Yang, L.; Liu, D.; Chen, J.; Fu, Q.; Xiong, Y.; Lin, F.; Xiang, B. Large-area synthesis of monolayer WSe₂ on a SiO₂/Si substrate and its device applications. Nanoscale **2015**, 7, 4193–4198.

- (92) Peng, G.-H.; Lo, P.-Y.; Li, W.-H.; Huang, Y.-C.; Chen, Y.-H.; Lee, C.-H.; Yang, C.-K.; Cheng, S.-J. Distinctive Signatures of the Spin-and Momentum-Forbidden Dark Exciton States in the Photoluminescence of Strained WSe₂ Monolayers Under Thermalization. Nano Lett. **2019**, 19, 2299–2312.
- (93) Barbone, M. et al. Charge-Tuneable Biexciton Complexes in Monolayer WSe₂. Nat. Commun. **2018**, 9, 3721.
- (94) Zinkiewicz, M.; Grzeszczyk, M.; Kipczak, Ł.; Kazimierzuk, T.; Watanabe, K.; Taniguchi, T.; Kossacki, P.; Babiński, A.; Molas, M. R. The Effect of Dielectric Environment on the Brightening of Neutral and Charged Dark Excitons in WSe₂ Monolayer. Appl. Phys. Lett. **2022**, 120, 163101.
- (95) Wu, F.; Qu, F.; MacDonald, A. H. Exciton Band Structure of Monolayer MoS₂. Phys. Rev. B **2015**, 91, 075310.
- (96) Qiu, D. Y.; Cao, T.; Louie, S. G. Nonanalyticity, Valley Quantum Phases, and Lightlike Exciton Dispersion in Monolayer Transition Metal Dichalcogenides: Theory and First-Principles Calculations. Phys. Rev. Lett. **2015**, 115, 176801.
- (97) Yu, H.; Liu, G.-B.; Gong, P.; Xu, X.; Yao, W. Dirac cones and Dirac saddle points of bright excitons in monolayer transition metal dichalcogenides. Nat. Commun. **2014**, 5, 3876.
- (98) Lin, J.-D.; Lo, P.-Y.; Peng, G.-H.; Li, W.-H.; Huang, S.-Y.; Chen, G.-Y.; Cheng, S.-J. Essential role of momentum-forbidden dark excitons in the energy transfer responses of monolayer transition-metal dichalcogenides. npj 2D Mater. Appl. **2023**, 7, 51.
- (99) Kresse, J., G. and Furthmüller Efficiency of Ab-Initio Total Energy Calculations for Metals and Semiconductors Using a Plane-Wave Basis Set. Comput. Mater. Sci. **1996**, 6, 15–50.
- (100) Kresse, G.; Furthmüller, J. Efficient Iterative Schemes for Ab Initio Total-Energy Calculations Using a Plane-Wave Basis Set. Phys. Rev. B **1996**, 54, 11169–11186.
- (101) Li, Y.; Chernikov, A.; Zhang, X.; Rigosi, A.; Hill, H. M.; van der Zande, A. M.; Chenet, D. A.; Shih, E.-M.; Hone, J.; Heinz, T. F. Measurement of the optical dielectric function of monolayer transition-metal dichalcogenides: MoS₂, MoSe₂, WS₂, and WSe₂. Phys. Rev. B **2014**, 90, 205422.
- (102) Parker, M. Physics of Optoelectronics; Optical Science and Engineering; CRC Press, 2018; Chapter 7.6, pp 518–520.
- (103) Blum, K. Density Matrix Theory and Applications; Springer Series on Atomic, Optical, and Plasma Physics; Springer Berlin Heidelberg, 2012; pp 43–47.
- (104) Babiker, M.; Bennett, C. R.; Andrews, D. L.; Dávila Romero, L. C. Orbital Angular Momentum Exchange in the Interaction of Twisted Light with Molecules. Phys. Rev. Lett. **2002**, 89, 143601.
- (105) Abdurazakov, O.; Li, C.; Shim, Y.-P. Formation of dark excitons in monolayer transition metal dichalcogenides by a vortex beam: Optical selection rules. Phys. Rev. B **2023**, 108, 125435.
- (106) Echeverry, J. P.; Urbaszek, B.; Amand, T.; Marie, X.; Gerber, I. C. Splitting between bright and dark excitons in transition metal dichalcogenide monolayers. Phys. Rev. B **2016**, 93, 121107.
- (107) Lu, Z.; Rhodes, D.; Li, Z.; Van Tuan, D.; Jiang, Y.; Ludwig, J.; Jiang, Z.; Lian, Z.; Shi, S.-F.; Hone, J.; others Magnetic field mixing and splitting of bright and dark

- excitons in monolayer MoSe₂. 2D Mater. **2019**, 7, 015017.
- (108) Schneider, L. M.; Esdaille, S. S.; Rhodes, D. A.; Barmak, K.; Hone, J. C.; Rahimi-Iman, A. Optical Dispersion of Valley-Hybridised Coherent Excitons with Momentum-Dependent Valley Polarisation in Monolayer Semiconductor. 2D Mater. **2020**, 8, 015009.
- (109) Shen, Y.; Wang, X.; Xie, Z.; Min, C.; Fu, X.; Liu, Q.; Gong, M.; Yuan, X. Optical Vortices 30 Years on: OAM Manipulation from Topological Charge to Multiple Singularities. Light Sci. Appl. **2019**, 8, 90.
- (110) Zhao, S.; Li, J.; Cai, Z. Generation of Three-Dimensional Polarization-Controlled Tunable Multiplex Focused Optical Vortex and Vector Vortex Beams Via Liquid Crystal Geometric Phase. Opt. Commun. **2023**, 537, 129401.
- (111) Rosales-Guzmán, C.; Ndagano, B.; Forbes, A. A Review of Complex Vector Light Fields and Their Applications. J. Opt. **2018**, 20, 123001.
- (112) Weber, R.; Michalowski, A.; Abdou-Ahmed, M.; Onuseit, V.; Rominger, V.; Kraus, M.; Graf, T. Effects of Radial and Tangential Polarization in Laser Material Processing. Phys. Procedia **2011**, 12, 21–30.
- (113) Toyoda, K.; Takahashi, F.; Takizawa, S.; Tokizane, Y.; Miyamoto, K.; Morita, R.; Omatsu, T. Transfer of Light Helicity to Nanostructures. Phys. Rev. Lett. **2013**, 110, 143603.
- (114) Zhao, Y.; Wang, J. High-Base Vector Beam Encoding/Decoding for Visible-Light Communications. Opt. Lett. **2015**, 40, 4843–4846.
- (115) Chen, R.; Agarwal, K.; Sheppard, C. J.; Chen, X. Imaging Using Cylindrical Vector Beams in a High-Numerical-Aperture Microscopy System. Opt. Lett. **2013**, 38, 3111–3114.
- (116) Kunin, A.; Chernov, S.; Bakalis, J.; Li, Z.; Cheng, S.; Withers, Z. H.; White, M. G.; Schönhense, G.; Du, X.; Kawakami, R. K.; Allison, T. K. Momentum-Resolved Exciton Coupling and Valley Polarization Dynamics in Monolayer WS₂. Phys. Rev. Lett. **2023**, 130, 046202.
- (117) Perdew, J. P.; Burke, K.; Ernzerhof, M. Generalized Gradient Approximation Made Simple. Phys. Rev. Lett. **1996**, 77, 3865–3868.
- (118) Giannozzi, P. et al. QUANTUM ESPRESSO: a Modular and Open-Source Software Project for Quantum Simulations of Materials. J. Phys. Condens. Matter **2009**, 21, 395502.